MAGNETIC METALS AND ALLOY NANOPARTICLES AS ELECTROMAGNETIC WAVE ABSORBERS

by

Shi Zhang

A thesis submitted to Johns Hopkins University in conformity with the requirements for the degree of Master of Science in Engineering

Baltimore, Maryland
May 2019

Abstract

With the increasing demand for both military defense and commercial applications, electromagnetic wave absorbers have been studied for years. Different materials can serve as absorbers, such as metal nanoparticles, Carbon-based materials and ferrites, etc.

Up to this point, most studies in nanomaterial electromagnetic wave absorption and/or electromagnetic interference have been “survey” studies in which a specific material of interest is studied, and results reported, rather than systematic studies in which important trends about fundamental material behavior can be deduced. Herein, we present organic solution synthesis routes towards preparation of a wide range of 10 nm magnetic metals and their alloyed nanoparticles. Through manipulation of the synthetic conditions we have been able to tune the metal compositions to a 1:1 ratio of M_1:M_2 alloy. We have evaluated the dependence of the permittivity (ε) and permeability (μ) of the nanoparticles on thickness, loading and alloying effect. The relationship between electromagnetic wave absorption properties and saturation magnetization were studied.

Our researches show that the magnetic loss is dominant in electromagnetic wave absorbing process in these nanoparticles and all the metal nanoparticles obtain better absorbing capacity than alloyed samples. This research is an important study in shedding light towards a better understanding of alloying effect on electromagnetic absorbing materials.

Acknowledgements

I would first thank my advisor, Dr. Chao Wang. It has been my pleasure to be his Master student. He did not only teach me nanoparticle technologies and electromagnetic wave absorption theory, he also taught me the cautious scientific attitude. His enthusiasm and unremittingness for research was very simulative. I appreciate all his contributions of time, ideas and financial support to make me finish these projects.

Next person I would like to give a specific appreciation is Dr. Michael Giroux, whom I worked with during these two years. He is more of an upperclassman, a colleague and a friend. I would like to express my deepest gratitude to him. The other members of the Wang Lab have also provided me abundant helps. I would like to thank Mukund Goyal, the master student working with our team for his advice and friendship. Also, I would like to thank Dr. Lei Wang, Fei Xu, Akshat Vij and Yuxuan Wang for advising on lab works and support for my life in Johns Hopkins University.

Lastly, I would like to thank my love ones for all their love, financial support, and encouragement they provided me in completing the master's degree.

Contents

List of tables

List of figures

1. Introduction

Radar absorbing materials (RAMs) play an important role in modern industry. For military defense, there is a growing demand for protecting military assets using stealth technology. It is important for the survivability of military vehicles that they are not detected until they are very close to their target. Methods of detecting the presence of hostile vehicles can be based on radar signals reflected from the threat, or thermal images arising from the temperature differences between the threat and the background, which can be detected and analyzed.[1] In general, vessels that are moving will be most vulnerable to detection by radar. Two different approaches exist to create “invisibility”: (a) Reduction of radar cross section (RCS) via shaping, which minimizes backscattered radar signals in the direction of the radar receiver, and (b) development of novel RAMs, which cover the surface of the vehicles or hardware, that absorb the incident radar signals (**Figure 1.1**). In morphing applications where the target shape changes dynamically, the first approach will have obvious limitations. Therefore, the design of adaptive RAMs becomes more important.[2]

Figure 1.1 Lockheed F-117 Nighthawk coated with RAMs. Source: Petrescu, R.V., et al., *Lockheed martin-a short review.* Journal of Aircraft and Spacecraft Technology, 2017. **1**(1).[3]

In addition to their use on stealth technology, RAMs are used in commercial microwave communications applications. Recently, RAMs have been used in civil and commercial environments to reduce radar scattering from large buildings at airports that can interfere with civil aviation radar systems. What's more, their single most prominent use is to absorb electromagnetic(EM) wave in portable electronic devices such as smart phones and mobile PCs to protect human bodies from exposure to electromagnetic pollution, which has been linked to an increased risk of developing cardiac/vascular diseases, cancer, or neural illnesses.[4-6] Therefore, great efforts have been made to develop high-efficiency EM absorbents including metallic materials, ferrites, carbon composites and nano-structured materials.

Magnetic materials have long been used as radar absorbers on aircrafts, e.g., in the form of iron ball paint. The absorber is usually applied by painting the metal surface with mixtures of carbonyl iron and polymer. This generates magnetic iron or ferrite particles in situ by decomposition and/or oxidation of iron carbonyl. Although this approach has been demonstrated to be successful in reduction of the RCS, it is still a challenge to obtain more efficient EM absorption materials, which possess strong absorption, light weight, thin thickness, and wide absorption frequency range. Metal nanoparticles as RAMs have received steadily growing interest because of their fascinating properties such as absorbing more microwave compared with the bulk or microsized counterparts.

This thesis presents the synthesis of six metallic/bimetallic nanoparticles as RAMs and the performance difference of each samples. We build up a model to predict and confirm the

behavior of these samples. This may bring about novel design and promote the application of RAMs in more comprehensive fields.

1.1 Nanoparticles synthesis

When materials go to the length scale of 1 – 100 nm, so-called nanomaterials, their properties can be dramatically changed from their bulk counterparts and bring about numerous novel phenomena. As a result, there lays great significance not only in understanding fundamental nano-science, but also in developing great potential applications in industry and human lives. It is well documented that the decreasing size at the nanoscale significantly increases the surface area of the material and gives rise to new properties. Nanoparticles can be classified as single, core-shell or composite nanoparticles depending on the composition of the material.[7] Typically, single nanoparticles consist of only one material; alternatively, the composite and core-shell particles are composed of two or more materials. Bimetallic nanoparticles are much more interesting because of their unique properties arising from synergistic or lattice strain effects between the two metals. Core-shell nanoparticles have been extensively studied by researchers as these nanoparticles have intriguing potential in electronics, biomedicine, pharmaceuticals, optics and catalysis.

Magnetic nanoparticles offer interesting current and future applications in high-density data storage, nanoscale electronics, sensors, and RAMs.[8-14] Magnetic properties of nanoparticles depend strongly on their size and shape in addition to their intrinsic magnetic characteristics, such as magnetic moment and magneto-crystalline anisotropy. Sufficiently

small nanoparticles have a single domain structure as opposed to larger particles, which can be divided into several domains with different magnetization orientations.[15]

Numerous approaches such as chemical, template-assisted and lithographic methods have been extensively investigated for the fabrication of a wide variety of magnetic nanostructures such as iron oxide, pure metal, metal alloys and core-shell structure, which have offered excellent size and shape control.[15]

Chemical synthesis of nanostructures has been achieved by thermal decomposition, co-precipitation, microemulsion and hydrothermal methods.[16] Thermal decomposition and hydrothermal approaches are much more advantageous because the particle size and shape can be effectively controlled (narrow distribution of the size of the particles) by changing the capping and reducing agents and with inexpensive materials and apparatus compared to other synthetic routes. Narrow distribution of the size of magnetic nanoparticles is important considering the fact that the magnetism of nanomagnets critically depends on the size of the particles and a polydisperse sample may result in varied magnetism, an undesirable situation in most of the applications.

Thermal decomposition method involves in the synthesis of monodisperse magnetic nanostructures by thermal decomposition of organometallic compounds such as acetylacetonates, carbonyls or cuproferronates in organic solvents in the presence of surfactants such as oleic acid and hexadecylamine.[17-20] The ratio of various precursors involved in the reaction governs the size and shape of nanostructures formed in the process. A general decomposition approach for the synthesis of size and shape controlled magnetic oxide nanocrystals has been reported by Peng and co-workers.[21] The technique is based on the

pyrolysis of metal fatty acid salts in the presence of corresponding fatty acids (lauric acid, myristic acid, decanoic acid, palmitic acid, oleic acid, stearic acid), a hydrocarbon solvent (e.g. octadecene), and activation reagents. Nanocrystals with very narrow size distribution and sizes tunable over a wide size range (3–50 nm) could be synthesized. Furthermore, the technique offered excellent control over the shape (spherical particles, cubes) of the nanocrystals.

Apart from metal oxide magnetic nanocrystals, thermal decomposition technique was also employed for the synthesis of shape-controlled metal nanocrystals. Magnetic nanoparticles of 3d transition metals (Co, Ni, Fe) were synthesized by introducing a reducing agent (oleylamine, borane tert-butylamine complex) into a hot solution of metal precursor and surfactant, which results in a single short nucleation event followed by slow growth process. Excellent control over the size and shape of the nanoparticles has been achieved by precisely choosing the temperature and metal precursor to surfactant and reducing agent ratio.[22-24] One noteworthy example, which subsequently led to significant developments, is the cobalt nanoplates synthesized by Alivisatos and co-workers using thermal decomposition of cobalt carbonyl precursor.[22] In subsequent studies, highly monodisperse cobalt and nickel nanorods have been synthesized using the thermal decomposition approach by various groups.[25-27] Such chemically synthesized nanostructures show minute magnetic interaction due to dilution and separation of nanoparticles in the solvent.

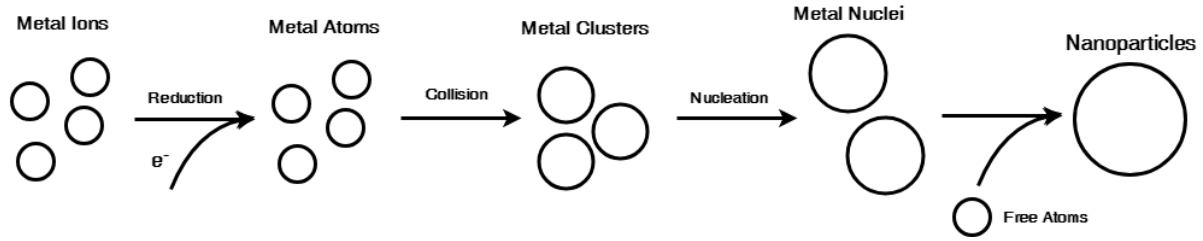

Figure 1.2 General mechanism of nanoparticle synthesis in organic solutions

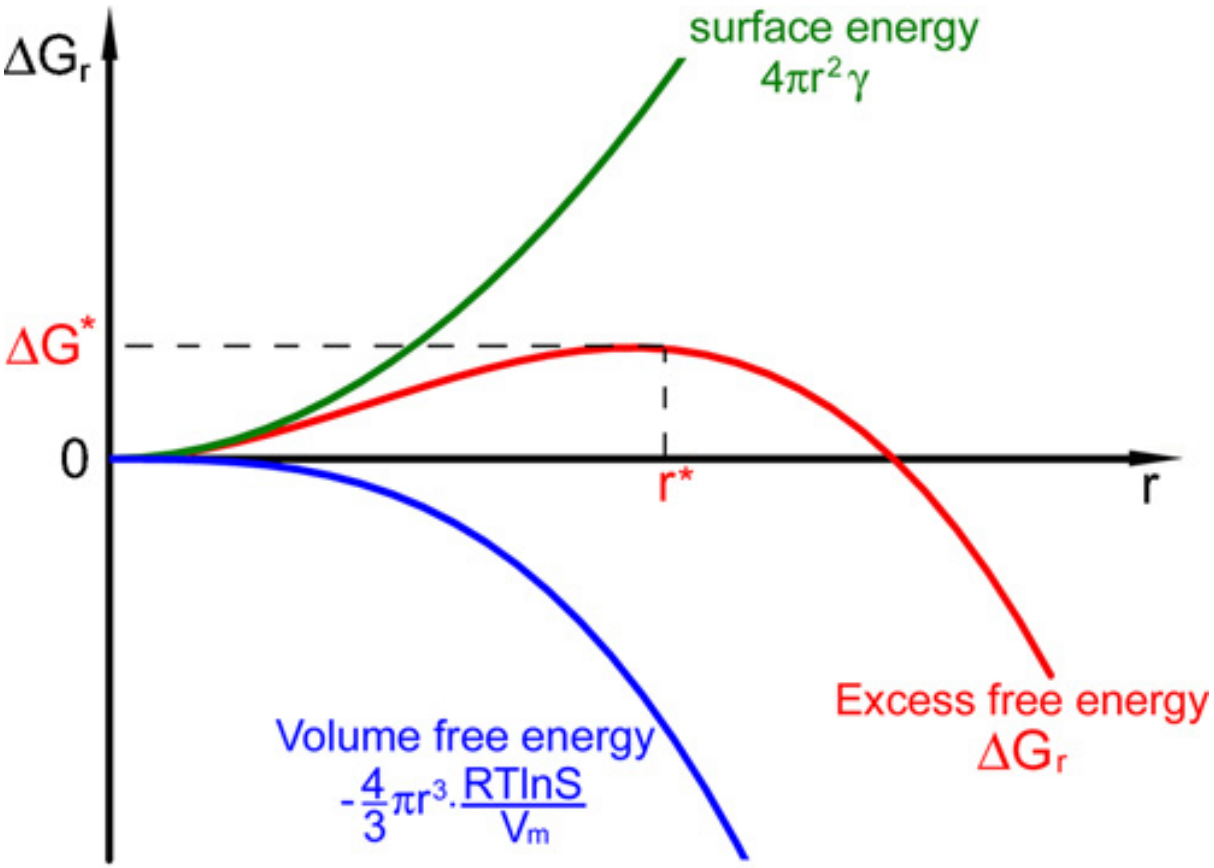

Figure 1.3 Overall excess free energy as a function of cluster size. Source: Peng, Z. and H. Yang, *Designer platinum nanoparticles: Control of shape, composition in alloy, nanostructure and electrocatalytic property.* Nano Today, 2009. **4**(2): p. 143-164.[28]

Figure 1.2 is showing the general mechanism of nanoparticle synthesis in organic solution. Also, **Figure 1.3** is showing the relationship between overall excess free energy with the size of nanoparticles. The nucleation process is an Ostwald ripening process. At initial stages, the

metal atoms form through the reduction of metal ions. The overall free energy is at the lowest stage. Then these metal atoms collide with each other to produce small clusters that are thermodynamically unstable, so the free energy starts to increase. After the clusters overcome a critical free energy barrier (G*) and become thermodynamically stable nuclei, these nuclei grow into nanoparticles at the consumption of free atoms in solution or unstable small clusters. After reaching the critical radius, the nanoparticles are hard to combine more atoms. The smaller cluster will consume the rest of the free atoms, so the overall systematic free energy will decrease.

1.2 Radar wave and RAMs

1.2.1 Definition of radar wave

In physics, electromagnetic radiation (EM radiation or EMR) refers to the waves (or their quanta, photons) of the electromagnetic field, propagating (radiating) through space, carrying electromagnetic radiant energy. It includes radio waves, microwaves, infrared, (visible) light, ultraviolet, X-rays, and gamma rays.

Classically, electromagnetic radiation consists of electromagnetic waves, which are synchronized oscillations of electric and magnetic fields that propagate at the speed of light. In homogeneous, isotropic media, the oscillations of the two fields are perpendicular to each other and perpendicular to the direction of energy and wave propagation, forming a transverse wave. The wavefront of electromagnetic waves emitted from a point source (such as a light bulb) is a sphere. The position of an electromagnetic wave within the

electromagnetic spectrum can be characterized by either its frequency of oscillation or its wavelength.

Electromagnetic waves are emitted by electrically charged particles undergoing acceleration, and these waves can subsequently interact with other charged particles, exerting force on them. EM waves carry energy, momentum and angular momentum away from their source particle and can impart those quantities to matter with which they interact. Electromagnetic radiation is associated with those EM waves that are free to propagate themselves ("radiate") without the continuing influence of the moving charges that produced them, because they have achieved sufficient distance from those charges.

1.2.2 RCS and RCS reduction

Exploitation of the electromagnetic spectrum for detection purposes extends from the ultra violet through visible, infrared, microwave and radio frequencies. The theory of physical optics has aided in the advancement of these detection methods. Conversely detection avoidance through camouflage, or signature reduction, exploits the same theory of physical optics to minimize reflections, emissions and hence detection. It is a combination of optics and materials that lead to signature reduction.[29]

The detectability of a target is measured in terms of the radar cross section (RCS), as shown in **Figure 1.4**. The radar cross section of a target is the projected area of a metal sphere that would scatter the same power in the same direction that the target does. RCS is related to the targets size, shape and the material from which it is fabricated and is a ratio of the incident and reflected power. RCS is normalized to the power density of the incident wave at the

target so that it does not depend on the distance of the target from the illumination source. RCS has been defined to characterize the target characteristics and not the effects of transmitter power, receiver sensitivity, and the position of the transmitter or receiver distance.

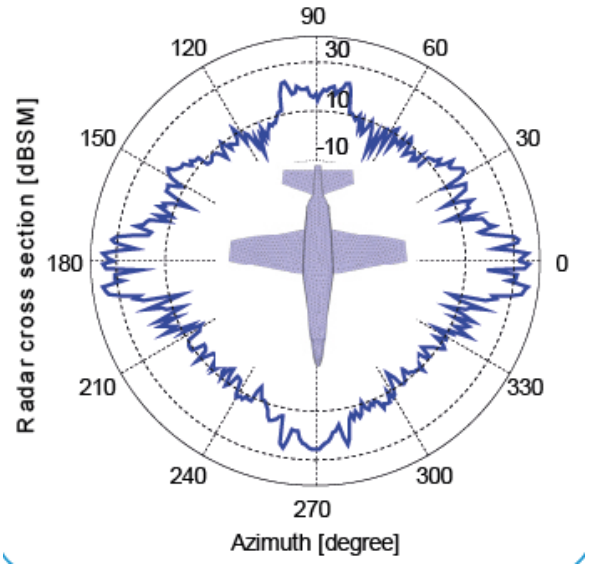

Figure 1.4 A typical diagram of radar cross section. Source: Barbosa, U.F., J.P.M.C. Costa, and R. Chaitanya. *Analysis of Radar Cross Section and Wave Drag Reduction of Fighter Aircraft*. in *proceedings of the AEROSPACE TECHNOLOGY CONGRESS*. 2016.[30]

There are only four basic techniques for reducing radar cross section:[31]

1. Shaping;

2. Radar absorbing materials;

3. Passive cancellation;

4. Active cancellation.

The two most practical and most often applied RCS reduction techniques are listed first, shaping and radar absorbing materials. When target surfaces are reshaped or reoriented to achieve the reduction, RCS reduction at one viewing angle is usually accompanied by an enhancement at another. If RAMs are used, the reduction is obtained by the dissipation of

energy within the material, thus leaving the RCS levels relatively unchanged in other directions.

1.2.3 Fundamental principle of RAMs

RAMs reduce the energy reflected back to the radar by means of absorption. Radar energy is absorbed through one or more of several loss mechanisms, which may involve the dielectric or magnetic properties of the material. The loss is actually the conversion of radio frequency energy into heat. The term ‘loss’ refers to the dissipation of power or energy, quite analogous to the way energy is consumed by a resistor when electrical current passes through it. Underlying the operation of RAMs is the fact that substances either exist or can be fabricated whose indices of refraction are complex numbers. In the index of refraction, which includes magnetic as well as electric effects, the imaginary component accounts for the loss in a material.

The main requirements are an effective electromagnetic wave impedance and good attenuation at the surfaces of a RAMs that result in a good match for the incoming signal once it penetrates into the material. At microwave frequencies, the loss is due to a number of effects on the atomic and molecular level.

For most practical electric absorbers, a majority of the loss is due to the finite conductivity of the material. The absorption by the dielectric materials depends on dielectric loss mechanisms, such as electronic/atomic polarization, orientation (dipolar) polarization, ionic conductivity, and interfacial or space charge polarization. On the other hand, for most magnetic absorbers at microwave frequencies, molecular friction experienced by molecules

in attempting to follow the alternating fields of an impressed wave within the domains is the principal loss mechanism. Magnetic loss mechanisms include Hysteresis Loop (from irreversible magnetization, which is negligible in a weak applied field), Domain Wall Resonance (which usually occurs in the frequency range 1-100 MHz), Natural Resonance, and Eddy Current losses.[2, 32, 33] In any event, it is customary to group the effects of all loss mechanisms into the permittivity (ε) and permeability (μ) of the material because the engineer is usually interested only in the cumulative effect.

Magnetic materials offer the advantage of compactness because they are typically a fraction of the thickness of dielectric absorbers. The basic lossy material is usually embedded in a matrix or binder such that the composite structure has the electromagnetic characteristics appropriate to a given range of frequencies.

1.2.4 Electromagnetic loss mechanisms

Several common usages exist for expressing the complex permittivity and permeability. Generally, we shall deal with the relative permittivity, ε_r, and relative permeability, μ_r, which are normalized by the free-space values, ε_0 and μ_0. The complex notation for ε_r and μ_r, is normally given as

$$\varepsilon_r = \varepsilon' - \mathrm{j}\varepsilon'' \qquad (1.1)$$

$$\mu_r = \mu' - \mathrm{j}\mu'' \qquad (1.2)$$

the prime (ε' and μ') and double prime (ε'' and μ'') superscripts represent the real and imaginary components of the complex numbers, respectively. The complex permittivity and permeability represent the dynamic dielectric and magnetic properties of materials. The real

components of the complex permittivity and permeability denote the storage capability of electric and magnetic energy. The imaginary components of them represent the absorption (loss) of the electric and magnetic energy. Even a small difference in permeability can affect the microwave absorption properties of the materials significantly.[34] Because the conductivity σ of electric absorbers is often the major loss mechanism[31], it is convenient to express the effect of the conductivity in terms of ε''. For that case, ε'' and σ are related by

$$\varepsilon'' = \frac{\sigma}{\omega\varepsilon_0} \tag{1.3}$$

where ω is the radian frequency. Equivalently, in polar notation,

$$\varepsilon_r = |\varepsilon_r| e^{-\mathrm{j}\delta_\varepsilon} \tag{1.4}$$

$$\mu_r = |\mu_r| e^{-\mathrm{j}\delta_\mu} \tag{1.5}$$

where δ_ε and δ_μ are the electric and magnetic loss tangents given by

$$\tan\delta_\varepsilon = \varepsilon''/\varepsilon' \tag{1.6}$$

$$\tan\delta_\mu = \mu''/\mu' \tag{1.7}$$

The index of refraction n is the ratio of the wavenumber describing wave propagation within the material to the free-space wavenumber and is to the geometric mean of the relative permittivity and permeability

$$n = k/k_0 = \sqrt{\mu_r\varepsilon_r} \tag{1.8}$$

where k is the wavenumber in the material, and $k_0 = \omega\sqrt{\mu_0\varepsilon_0}$ is the free-space wavenumber. Similarly, μ_r and ε_r also define the intrinsic impedance, Z, of the material

$$Z = Z_0\sqrt{\mu_r/\varepsilon_r} \tag{1.9}$$

where Z_0 is the impedance of free space, 120π, which is approximately 377Ω.

The intrinsic impedance is the impedance value seen by a normally incident wave on a semiinfinite slab of a material. In practical applications, a layer of dielectric will often be backed by a conducting surface. For that case a transmission line analysis can be performed to find the effective input impedance at the front face of the layer.

For a flat metallic surface coated with a layer of dielectric material, the normalized input impedance Z_{in} is given by

$$Z_{in} = \sqrt{\mu_r/\varepsilon_r}\tanh(\mathrm{j}k_0 d\sqrt{\mu_r\varepsilon_r}) = \sqrt{\mu_r/\varepsilon_r}\tanh(\mathrm{j}\frac{2\pi f d\sqrt{\mu_r\varepsilon_r}}{c}) \qquad (1.10)$$

where d is the thickness of the RAMs layer, c is the speed of light, $f = \omega/2\pi$ is the frequency. This formula applies to a wave striking the surface at normal incidence, and it becomes more complicated when the wave arrives at oblique angles. The normalized impedance can be used to calculate the reflection coefficient R:

$$R = \frac{Z_{in} - 1}{Z_{in} + 1} \qquad (1.11)$$

R, like Z_{in}, is a complex number, but has a magnitude between 0 and 1.

In discussing reflection coefficients, it is customary to ignore the phase angle and to refer only to the "voltage" amplitude R_L, so that the power reflection in decibels is

$$R_L = 20log\left|\frac{Z_{in}-1}{Z_{in}+1}\right| \qquad (1.12)$$

The objective of RAMs design is to produce a material for which R_L remains as small as possible over as wide a frequency range as possible. It should be noted that unless the material has some loss, the amplitude of the reflection coefficient will be controlled entirely by the phase and amplitude relationship between the portion of the incident wave reflected at the front surface and the portion returning via reflections at the backing surface.

1.3 Transmission line theory

1.3.1 Basic principle

The most basic information needed in the electrical design of the absorber is the electromagnetic properties of the materials we expect to use to manufacture it. Bulk materials are characterized by their relative permeabilities and permittivities, whereas thin sheets are more conveniently characterized by complex impedances. Permeability and permittivity are recognized as complex quantities, and we typically normalize these values with respect to the corresponding free-space values. The impedance of a thin sheet is also a complex quantity (a resistance and a reactance).

The relative permeability and permittivity of test samples are most accurately measured in small fixtures that are actually short sections of transmission lines. This minimizes the escape of energy from the system, thus reducing the risk that energy losses might be attributed to nonexistent losses within the test sample.

The transmission line is a basic device used to measure the electromagnetic properties of materials because the theory of wave propagation within the line is well understood and radio frequency (RF) energy is confined within the system. A sample holder — a short section of transmission line — is loaded with a test sample machined to fit the line, and the reflection of RF energy from it, or the transmission of RF energy through it, or both, are measured. Because the dependence of the two measured quantities on the electromagnetic properties of the material in the line is known, those properties may be extracted by appropriate manipulation of the test data.

During the test, we may launch a signal down the line and measure the signal at the far end. The reflection coefficient (r) of an electromagnetic wave entering from free space into a material with flat surface can be written as

$$r = \frac{Z \tanh \gamma d - Z_0}{Z \tanh \gamma d + Z_0} \tag{1.13}$$

with

$$\gamma = \sqrt{\mathrm{j}\omega\mu(\sigma + j\omega\varepsilon)} \tag{1.14}$$

Here γ is the complex propagation constant. When there are no ohmic losses in the line, γ is the imaginary number $-\mathrm{j}k = -\mathrm{j}2\pi/\lambda$ with λ is the wavelength of the signal as measured within the material in the line, which describes the shift in the phase of the signal as it travels along the line; in the absence of loss, there is no change in its amplitude. If there are energy losses in the line, due either to the finite conductivity of the conductors of the line or losses in the material filling it, γ and k are complex quantities.

To maximize the electromagnetic wave absorption, the ideal case is to have r in equals to zero, namely zero reflection, which requires the so-called impedance matching condition

$$Z \tanh \gamma d = Z_0 \tag{1.15}$$

For typical magnetic absorbers, the conductivity σ is small at the frequency of interest in most applications so

$$\sqrt{\mu/\varepsilon} \tanh\left(\mathrm{j}\omega d\sqrt{\mu\varepsilon}\right) = \sqrt{\mu_0/\varepsilon_0} \tag{1.16}$$

which is a complicated complex equation for which analytical solution is challenging. If the dielectric loss of the magnetic absorber can be assumed to be small ($\varepsilon'' \ll \varepsilon'$) and the magnetic loss is large ($\mu'' \gg \mu'$), it can be further simplified as

$$\omega\mu'' d = Z_0 \tag{1.17}$$

In our work, we used the transverse electromagnetic line for the evaluation of the electromagnetic properties. The electric and magnetic fields inside the TEM line are both transverse to the length of the line, as suggested in **Figures 1.5**, with the result that energy propagates within the line just as it would in an unbounded medium made of the same material filling the line.

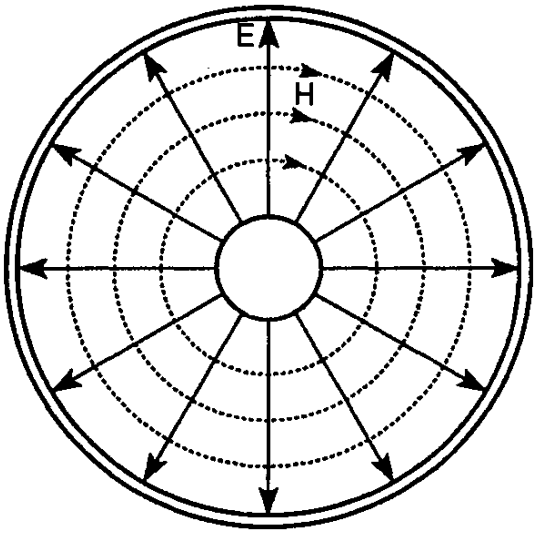

Figure 1.5 Electric field lines are radial and magnetic field lines are circumferential in the coaxial transmission line. Energy is constrained between the inner and outer conductors and does not escape the line. Source: Knott, E.F., J.F. Schaeffer, and M.T. Tulley, *Radar cross section*. 2004: SciTech Publishing.[31]

Because electromagnetic energy is confined between the conductors of the coaxial line, the coaxial line is the most common system used for measuring the properties of uniform test samples.[31] The samples should be fabricated to fit snugly within the sample holder, making good contact with all conducting surfaces. Almost all sample holders are designed for easy removal from the test set-up so that the samples may be inserted into or tapped out of the holder with minimum disturbance to the rest of the system.

1.3.2 The network analyzer and the scattering matrix

The network analyzer is a basic tool in the measurement of the properties of radar materials. The basic instrument compares an unknown signal with a reference signal of the same frequency, and its output is a signal or indication of the amplitude and phase of the unknown signal. To preserve the coherence of this indication, the analyzer demands that the reference signal be derived from the same source used to excite the device under test, usually a two-port network. Any of several plug-in test sets are offered that expedite specific kinds of measurement, such as the reflection and transmission characteristics of two-port devices or their scattering matrices (S-parameters).

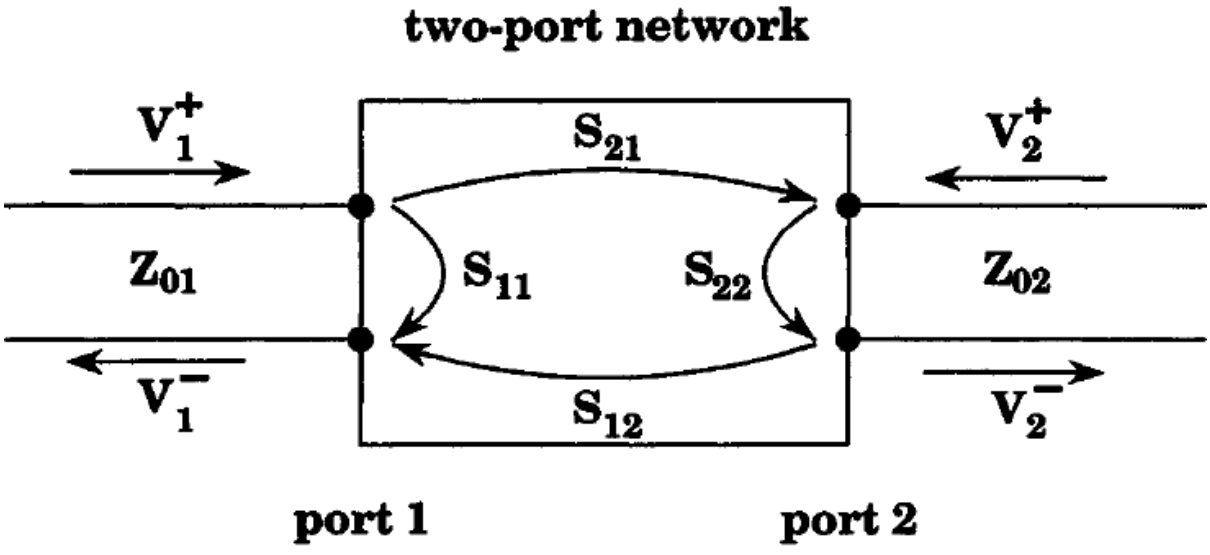

Figure 1.6 Four complex numbers characterize the scattering-matrix representation of two-port networks. Source: Knott, E.F., J.F. Schaeffer, and M.T. Tulley, *Radar cross section*. 2004: SciTech Publishing.[31]

The basic two-port representation now favored for materials testing is the S-parameter configuration shown in **Figure 1.6**. The complete characterization of the scattering matrix of

an unknown device demands the measurement of no fewer than eight quantities: the amplitude and phase (or the real and imaginary parts) of the four scattering-matrix parameters. If the device is passive and reciprocal, however, as is the case for the materials we seek to measure, it can be shown that $S_{12} = S_{21}$ and $S_{11} = S_{22}$. Therefore, we need measure only two complex parameters (S_{11} and S_{21}) to characterize the material. Electromagnetic constitutive parameters for the coated fabrics (ε', ε'', μ', μ'') were calculated from the measured S-parameters (S_{11} and S_{21}) using the Nicolson-Ross-Weir technique [32, 35]:

$$S_{11} = \frac{u(1-w^2)}{u^2-w^2} \tag{1.18}$$

$$S_{21} = \frac{w(u^2-1)}{u^2-w^2} \tag{1.19}$$

where

$$u = \frac{1+y_r}{1-y_r} \tag{1.20}$$

$$y_r = \sqrt{\varepsilon_r/\mu_r} \tag{1.21}$$

We can get

$$w^2 = \frac{u(1-uS_{11})}{u-S_{11}} \tag{1.22}$$

$$u^2 + 2uQ + 1 = 0 \tag{1.23}$$

where

$$Q = [(S_{21})^2 - (S_{11})^2 - 1]/2S_{11} \tag{1.24}$$

From **Equation (1.22)** and **(1.23)**, we can get two solutions for u:

$$u = -Q \pm (Q^2 - 1)^{1/2} \tag{1.25}$$

which requires complex arithmetic to solve, as Q is a complex number. The negative option of u happens to be the one we need, from which we may calculate a number U:

$$U = \frac{u-1}{u+1} \tag{1.26}$$

Combined with (1.20) and (1.21), we can get:

$$\sqrt{\varepsilon_r/\mu_r} = U \tag{1.27}$$

$$W = \frac{u(1-uS_{11})}{u-S_{11}} \tag{1.28}$$

Therefore,

$$\sqrt{\mu_r\varepsilon_r} = \frac{\ln W}{-\mathrm{j}2k_0t} \tag{1.29}$$

$$\varepsilon_r = \frac{U\ln W}{-\mathrm{j}2k_0t} \tag{1.30}$$

$$\mu_r = \frac{\ln W}{-\mathrm{j}2k_0tU} \tag{1.31}$$

where *t* is the transmission line length.

2. Experimental section

For bimetallic alloy nanoparticles, a thermal decomposition reaction of metallic salts is direct and convenient. As for reaction systems, a non-aqueous phase with surfactants and proper reducing agents for respective metals are necessary.[36] Reducing agents are critical for synthesis in different metal salts because they always control both reaction rate and nanoparticle sizes altogether. Conventional reducing agents for metallic are sodium borohydride and hydrazine. However, the reduction of iron ions by borohydrides in aqueous solution may produce various compounds, such as $Fe_{65}B_{35}$, rather than pure metal or metal alloy nanoparticles.[37] In addition, the aqueous reaction environment practically limits the reaction temperature, and often leads to the formation of nanoparticles with an amorphous structure. Nonaqueous synthetic routes which use high boiling-point organic solvents as reaction media provide an alternative approach to prepare metal and metallic alloy nanoparticles. The high reaction temperature provided by the solvent often leads to a highly crystalline structure, and therefore provides improved magnetic properties.

For all samples synthesized in our project, their sizes were around 10nm, which indicated the superparamagnetism and sing domain properties. The superparamagnetic transition depends therefore on the nature of the material, the size and the shape of the nanoparticles and can be described in terms of the smallest size of the nanoparticles (when they are still blocked at room temperature) or in terms of the temperature at which the superparamagnetic transition occurs for a given average size of the particles. **Figure 2.1** shows that how the critical size for superparamagnetic transition (D_{sp}) depends on the type of the material for several common ferromagnetic materials. It demonstrates also another transition between a single-domain and

polydomain state, D_{crit}.[12] As follows from this consideration, nanoparticles of 10–15 nm in diameter with effective anisotropies typical for 3d ferromagnets have the blocking temperature[38] much below the room temperature.[15] For such a case the individual particle dipoles are randomly oriented due to thermal fluctuations and hence, a collection of such nanoparticles does not possess a net magnetic moment unless an external magnetic field aligning the individual dipole moments of the nanoparticles is applied.

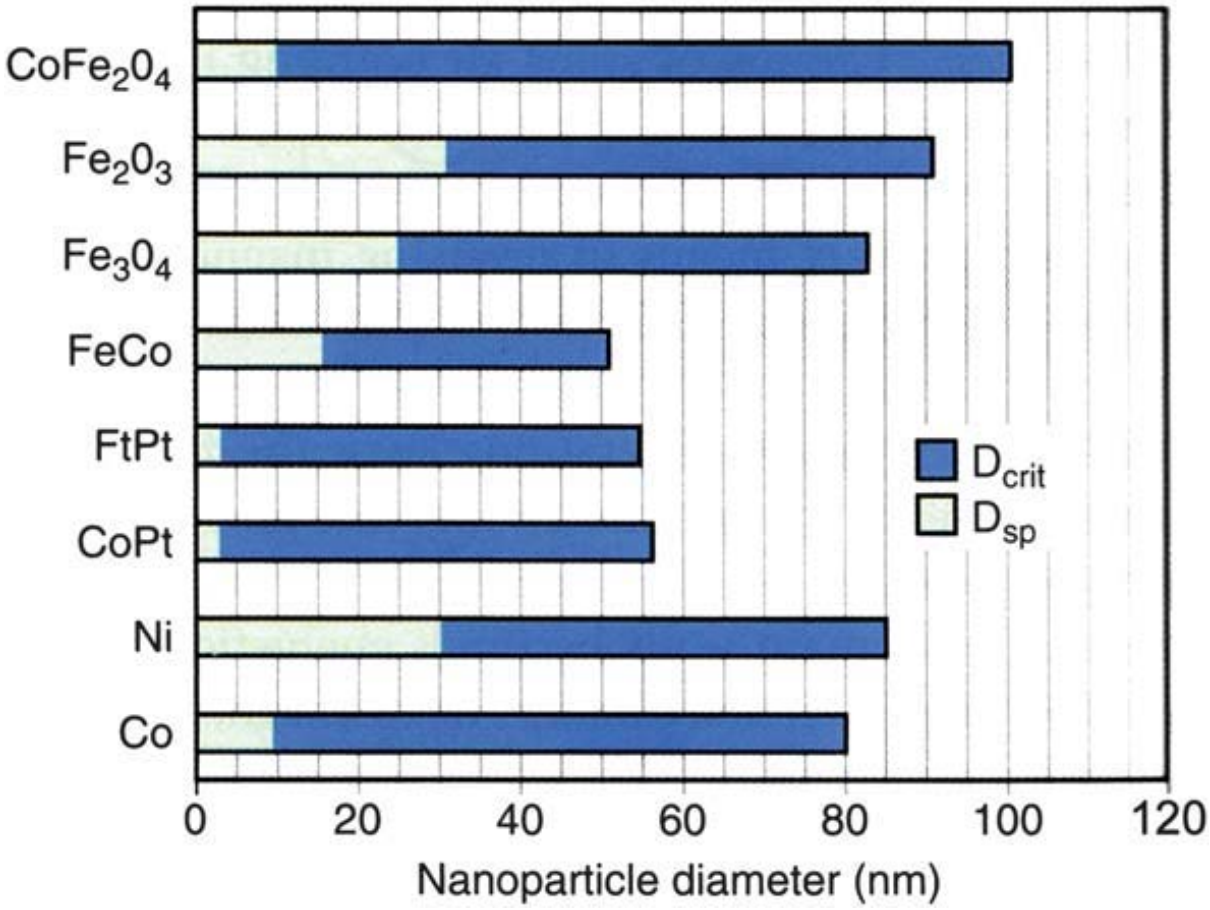

Figure 2.1 Single domain size D_{crit} and superparamagnetic limit at room temperature, D_{sp} for common ferromagnetic materials. Source: Singamaneni, S., et al., *Magnetic nanoparticles: recent advances in synthesis, self-assembly and applications.* Journal of Materials Chemistry, 2011. **21**(42): p. 16819-16845.[15]

2.1 Setup

A typical system for the thermal decomposition of metal precursors to synthesize nanoparticles is shown in **Figure 2.1**. Inert gas (Argon) was introduced by standard Schlenk lines to protect the reaction from oxygen and moisture. Reaction precursor, reducing agents, solvent and surfactants were added into a flask (50 ml) for growth. The mixture was stirred by a Teflon magnetic bar on a Fisherbrand™ Isotemp™ Stirrer throughout the whole reaction. The flask was heated by a heating mantle powered by a voltage controller.

2.2 Synthesis

Chemicals. Iron Pentacarbonyl ($Fe(CO)_5$), Dicobalt Octacarbonyl ($Co_2(CO)_8$), Cobalt(II) Acetylacetonate ($Co(acac)_2$), 1-Octadecene (ODE), Oleyl amine (OAm), Oleic Acid (OA), 1,2-Dichlorobenzene (DCB), Dioctylamine (DOA), Trioctylphosphine(TOP) and Borane tert-butylamine(BTB) were purchased from Sigma-Aldrich, Iron(III) Acetylacetonate ($Fe(acac)_3$) and Nickel(II) Acetylacetonate ($Ni(acac)_2$) were purchased from Strem Chemicals Inc.
All synthesis procedures were adapted and modified from a previous report.

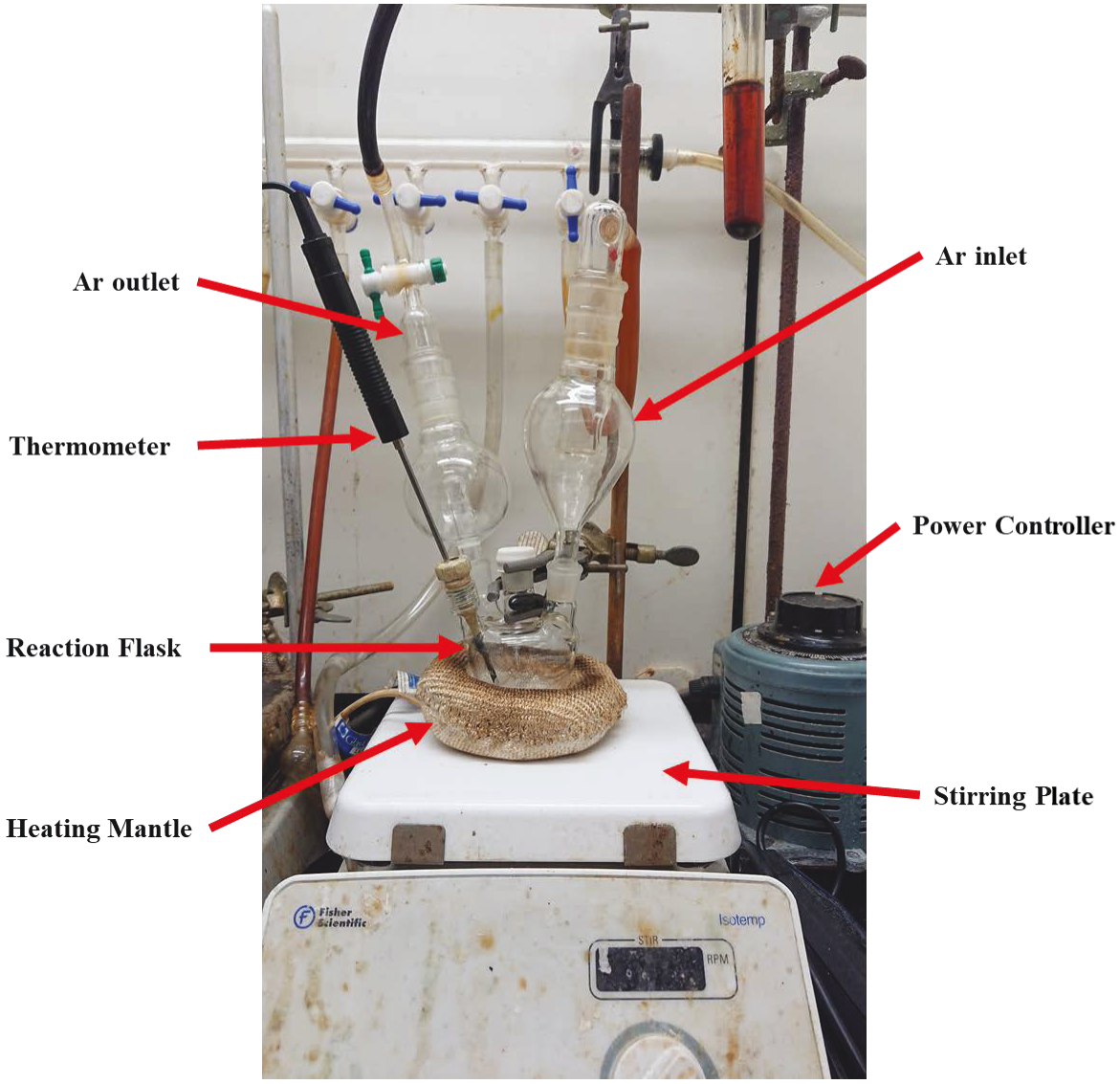

Figure 2.2 Experiment setup for nanoparticles synthesis.

Synthesis of 10nm Fe nanoparticles.

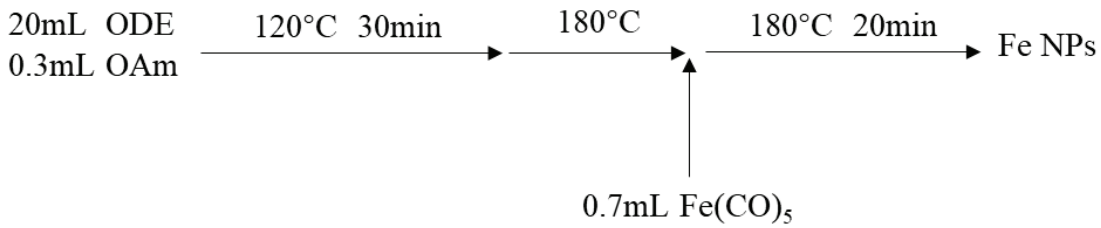

Figure 2.3 Schematic illustration of the synthetic route for Fe nanoparticles

10 nm Fe nanoparticles were synthesized by the decomposition of $Fe(CO)_5$. In a typical synthesis, 20mL ODE and 0.3mL OAm were heated at 120°C for 30 min to remove water and impurities from the mixture. 0.7mL $Fe(CO)_5$ was injected at 180°C and the mixture was refluxed for 20 min. After cooling down, the mixture was diluted with isopropanol and centrifuged at 10000 rpm for 5 min to precipitate out the iron nanoparticles from solution. The nanoparticles were then re-dispersed in hexane.

Synthesis of 10nm Co nanoparticles.

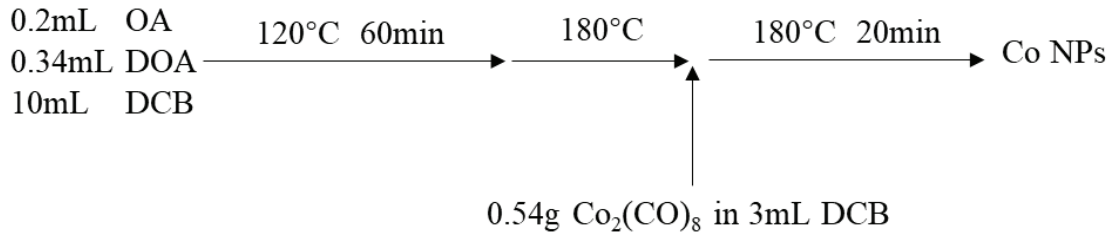

Figure 2.4 Schematic illustration of the synthetic route for Co nanoparticles

10 nm Co nanoparticles were synthesized by the decomposition of $Co_2(CO)_8$. In a typical synthesis, 0.2mL Oa, 0.34mL DOA and 10mL DCB were heated 120°C for 60 min to remove water and impurities from the mixture. 0.54g $Co_2(CO)_8$ was dissolved in 3mL DCB in glovebox and then injected into the mixture at 180°C. The mixture was refluxed for 20 min. After cooling down, the mixture was diluted with ethanol and centrifuged at 10000 rpm for 5 min to precipitate out the cobalt nanoparticles from solution. The nanoparticles were then re-dispersed in hexane.

Synthesis of 10nm Ni nanoparticles.

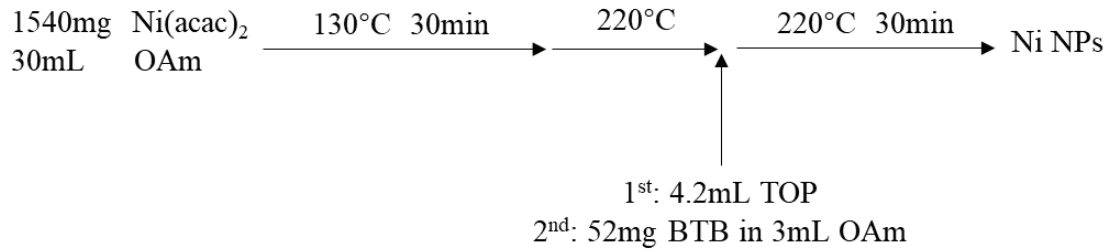

Figure 2.5 Schematic illustration of the synthetic route for Ni nanoparticles

10 nm Ni nanoparticles were synthesized by the decomposition of $Ni(acac)_2$. In a typical synthesis, 1540mg $Ni(acac)_2$ was dissolved in 30mL OAm and heated at 130°C for 30 min. 4.2mL TOP was then injected to the solution at 220°C, followed by the injection of 52mg BTB dissolved in 3mL OAm. The whole solution remained 220°C for 30 min and then after cooling down, the solution was washed twice with ethanol and centrifuged at 10000 rpm for 5 min to precipitate out the nickel nanoparticles from solution. The nanoparticles were then re-dispersed in hexane.

Synthesis of 10nm FeCo nanoparticles.

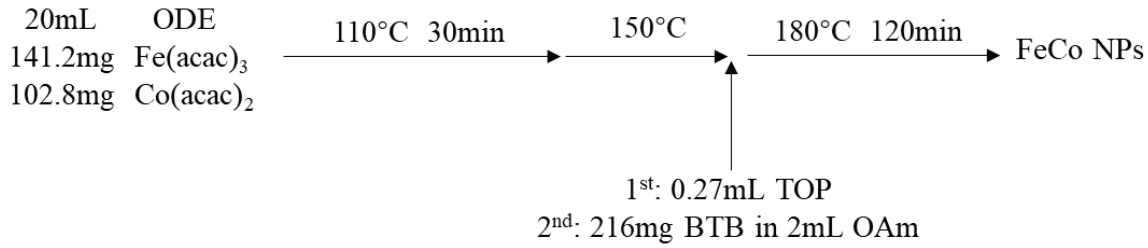

Figure 2.6 Schematic illustration of the synthetic route for FeCo nanoparticles

10nm FeCo nanoparticles were synthesized by the decomposition of $Fe(acac)_3$ and $Co(acac)_2$. In a typical synthesis, 141mg $Fe(acac)_3$ and 102mg $Co(acac)_2$ were dissolved in 20mL ODE

and heated at 130°C for 30 min. 0.27mL TOP was injected to the solution at 150°C, followed by the injection of 22mg BTB dissolved in 2mL OAm. The whole solution was refluxed at 180°C for 120 min. After cooling down, the solution was diluted with ethanol and centrifuged at 10000 rpm for 5 min to precipitate out the FeCo nanoparticles from solution. The nanoparticles were then re-dispersed in hexane.

Synthesis of 10nm $FeNi_2$ nanoparticles.

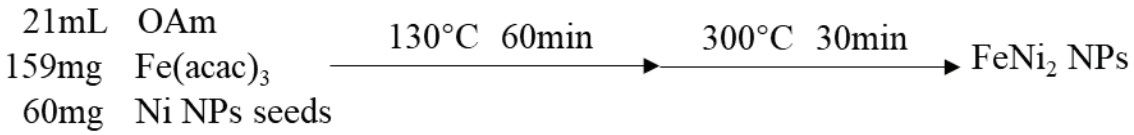

Figure 2.7 Schematic illustration of the synthetic route for $FeNi_2$ nanoparticles

10nm $FeNi_2$ nanoparticles were synthesized by the decomposition of $Fe(acac)_3$ and pure Ni nanoparticles. In a typical synthesis, 60mg Ni nanoparticles from the method above and 159mg $Fe(acac)_3$ were dissolved in 21mL OAm and heated at 130°C for 60 min. The mixture was then refluxed at 300°C for 30 min. After cooling down, the solution was diluted with acetone and hexane mixture and centrifuged at 10000 rpm for 5 min to precipitate out the $FeNi_2$ nanoparticles from solution. The nanoparticles were then re-dispersed in hexane.

Synthesis of 10nm CoNi nanoparticles.

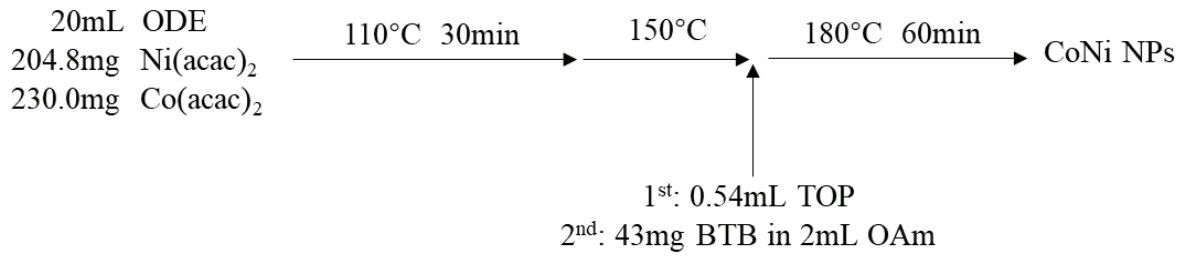

Figure 2.8 Schematic illustration of the synthetic route for CoNi nanoparticles

10nm CoNi nanoparticles were synthesized by the decomposition of $Co(acac)_2$ and $Ni(acac)_2$. In a typical synthesis, 230mg $Co(acac)_2$ and 205mg $Ni(acac)_2$ were dissolved in 20mL ODE and heated at 110°C for 30 min. 0.54mL TOP was injected to the solution at 150°C, followed by the injection of 43mg BTB dissolved in 2mL OAm. The whole solution was refluxed at 180°C for 60 min. After cooling down, the solution was diluted with ethanol and centrifuged at 10000 rpm for 5 min to precipitate out the CoNi nanoparticles from solution. The nanoparticles were then re-dispersed in hexane.

2.3 Characterization

Transmission electron microscopy (TEM) imaging was acquired on a 120 kV FEI Tecnai 12 TWIN microscope. X-ray diffraction (XRD) patterns were collected on a PAN analytical X'Pert Powder X-Ray Diffractometer equipped with a Ci K radiation source. Energy dispersive spectroscopy (EDS) to perform elemental analysis was performed on a JEOL 6700F field emission electron scanning microscope.

2.4 Electromagnetic wave absorption Studies

All 10nm metal/alloys composite wax/nanoparticle samples were prepared in 20 mL scintillation vials by dispersing the appropriate amounts of paraffin wax and nanoparticles in toluene to achieve nanoparticle volume fractions ranging from 15% to 40% and slowly evaporating the solvent in a glovebox to avoid any oxidation and to create a uniformly dispersed composite matrix. The resulting composites were then molded into a toroidal shape, as **Figure 2.8** shows, using a Teflon mold with an outer diameter of 6.98 mm, inner diameter of 3.03 mm and thickness ranging from 1 to 6 mm for the microwave measurements. The toroid was strung on the 7mm, 25OHM center conductor and the loaded into the corresponding mismatch airline (**Figure 2.9** – **2.10**). The complex permittivity and permeability of the composite samples were measured using a Keysight FieldFox N9918A Microwave Analyzer in the 2 – 18 GHz region and the reflection loss was calculated used the measured permittivity and permeability (**Figure 2.11**）.

Figure 2.9 Toroidal-shaped composites

Figure 2.10 7 mm, 25 OHM Mismatch airline and conducting rod

Figure 2.11 Toroid matrix loaded on conducting rod and in airline

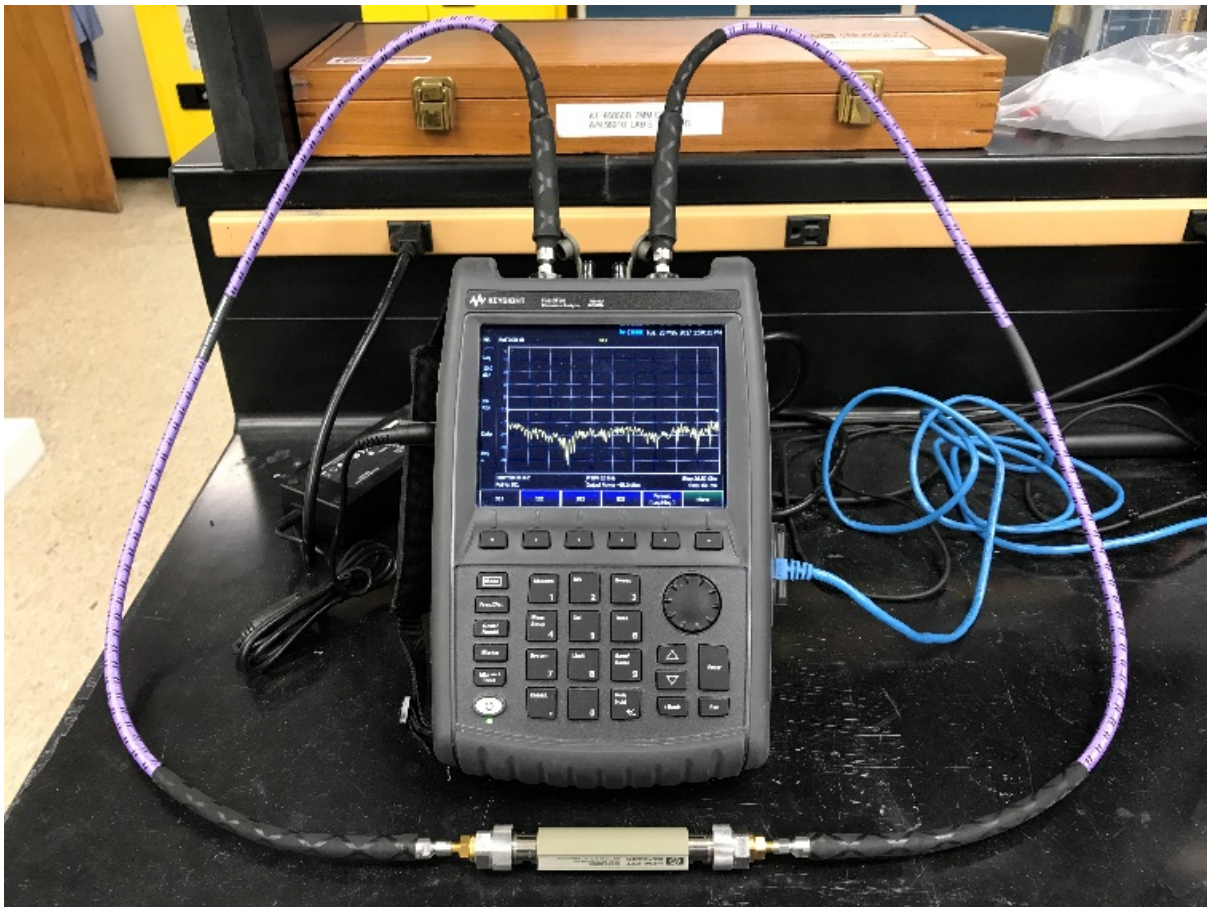

Figure 2.12 Keysight FieldFox N9918A Microwave Analyzer performing VNA test.

3. Result and discussion

3.1 Materials characterization

Metal/alloys (Fe, Co, Ni, FeCo, $FeNi_2$, CoNi) nanoparticles of size around 10 nm are shown in TEM images in **Figure 3.1**.

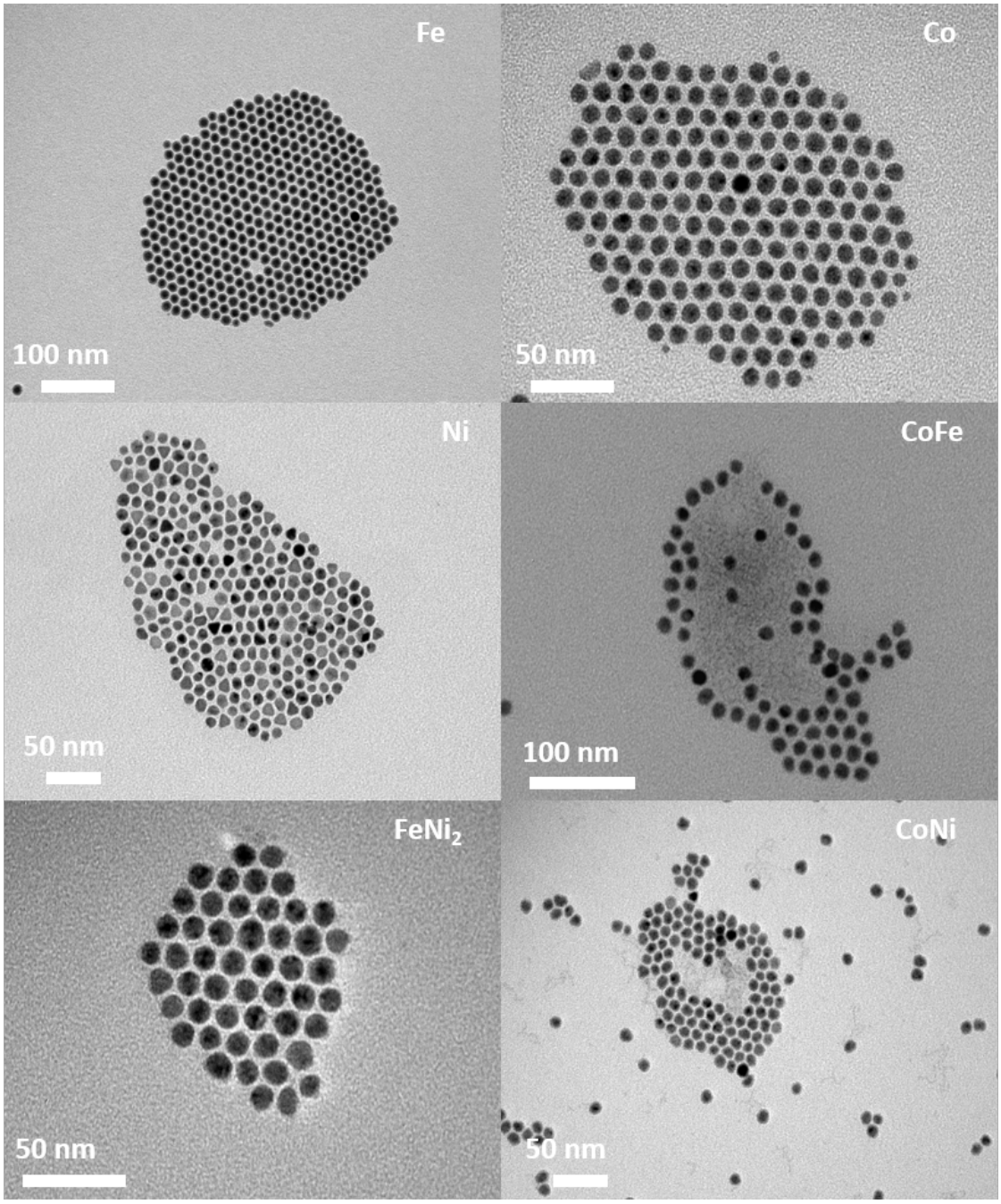

Figure 3.1 TEM images of metal/bimetallic alloy nanoparticles

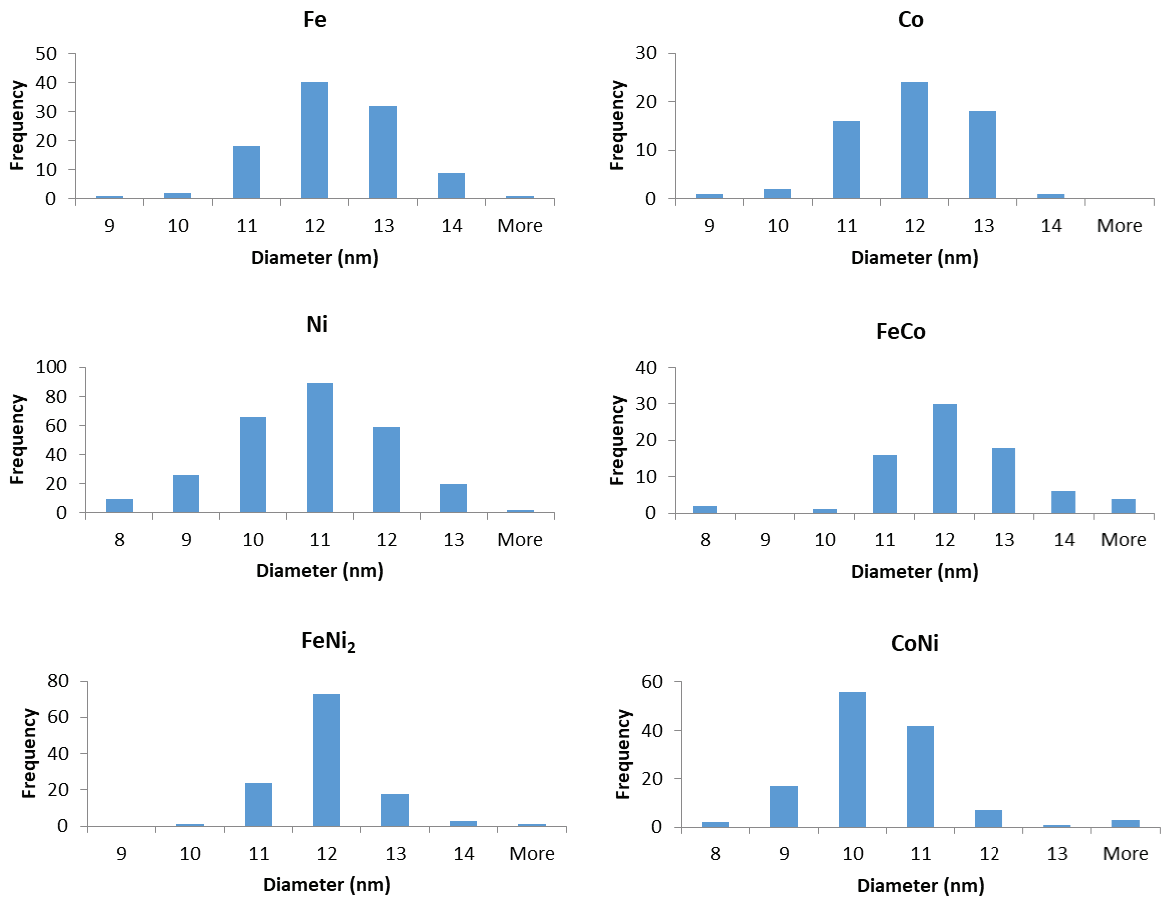

Figure 3.2 Size distribution of all nanoparticles

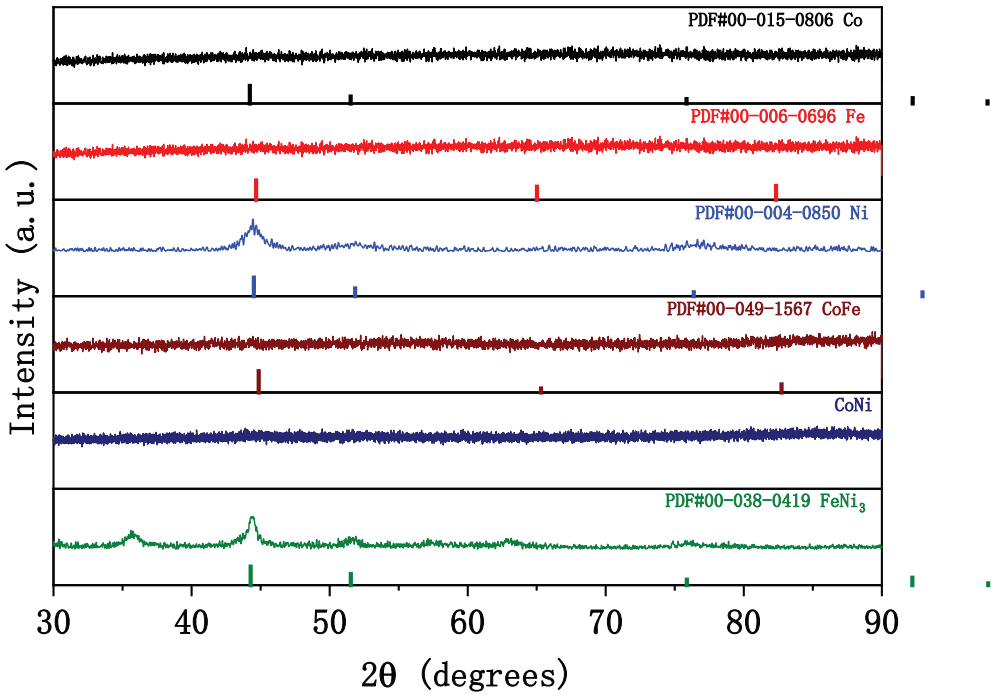

Figure 3.3 XRD patterns of all nanoparticles

All synthesized nanoparticles show a sphere-like morphology. Through size distribution analysis shown in **Figure 3.2**, mean diameters have been determined to be 11.76 nm (Fe), 11.44 (Co), 10.54 nm (Ni), 11.71 nm (CoFe), 11.52 nm ($FeNi_2$) and 10.31 nm (CoNi).

Figure 3 presents the typical XRD pattern for the various nanoparticles. Except for Ni and $FeNi_2$, all other nanoparticles show no obvious peaks and thus amorphous patterns. Ni nanoparticles' pattern is highly agreed with JCPDS No. 00-004-0850 (Ni) and no other diffraction peaks besides those corresponding to the appropriate ones were observed, which indicates nearly no oxidation and high purity of the products. $FeNi_2$ has several peaks as JCPDS NO. 00-038-0419 ($FeNi_3$) shows although not exactly the same.

Table 1 provides the EDS results of each samples, which confirms the elemental composition of each sample.

Table 1. EDS data for each sample

Material	**Mass % M_1**	**Mass % M_2**	**Atomic % M_1**	**Atomic % M_2**	**Ratio M_1:M_2**
Fe	100	-	100	-	-
Co	100	-	100	-	-
Ni	100	-	100	-	-
CoFe	50.25	49.75	48.91	51.09	1:1
CoNi	49.30	50.70	49.21	50.79	1:1
$FeNi_2$	34.60	65.40	35.74	64.26	1:2

3.2 Magnetic properties

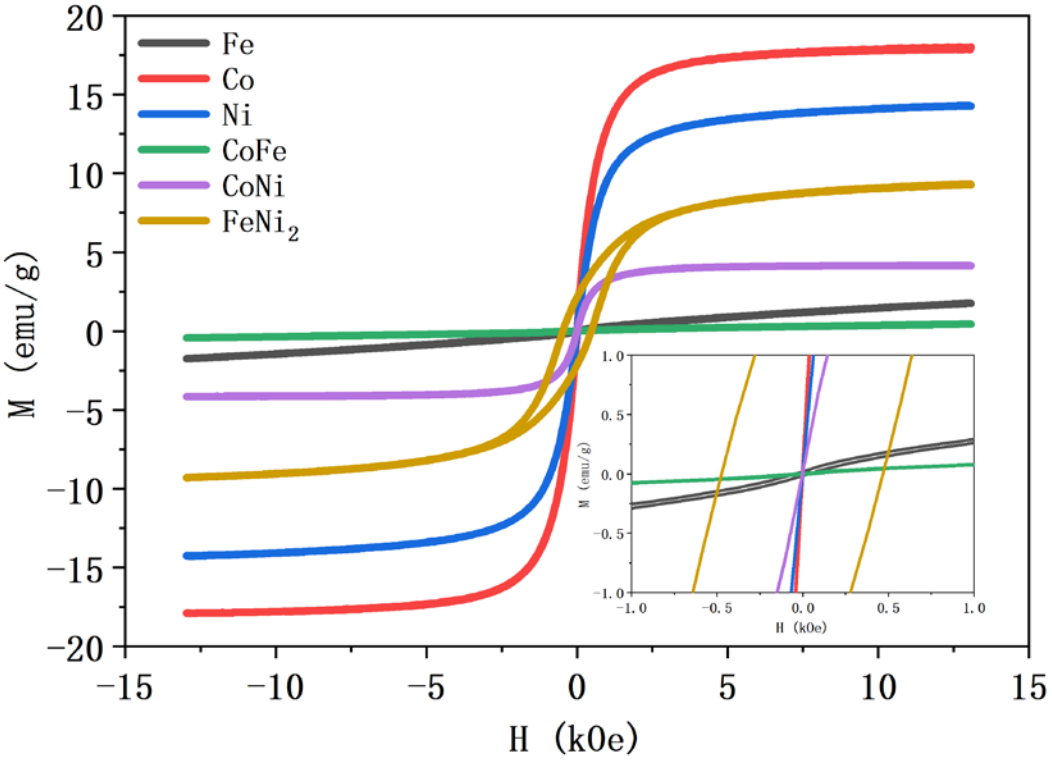

Figure 3.4 Magnetic hysteresis loops of metallic/bimetallic nanoparticles. Inset shows a close-up of the region around zero.

Figure 3.4 displays the magnetic hysteresis loops of all the as-synthesized metallic and bimetallic nanoparticles. The saturation magnetization values (M_s) vary from sample to sample and were determined by assuming $M(H) = M_s + X_dH$ (X_d being the high field susceptibility) at high field and extrapolating the M(H) curve to zero field (i.e. $H = 0$).[39] M_s values were found to be 1.76 (Fe), 18.0039 (Co), 14.25888 (Ni), 0.44026 (CoFe), 4.14939 (CoNi), and 9.27003($FeNi_2$) emu/g. All of these values are much lower than that of the corresponding bulk metals or alloys (50 – 250 emu/g), which is expected due to the nanoscale size of the materials as established in previous literature.[40] However, among all samples,

Fe and CoFe show a paramagnetic behavior with especially low M_s, which is uncommon.[41, 42] This may come from experimental errors since these nanoparticles should be superparamagnetic under the experimental condition. The $FeNi_2$ sample shows a loop and indicates the ferromagnetism. Co, Ni, and CoNi display superparamagnetic behavior. M_s strongly depends on the composition, particle size, surface anisotropy in different shapes and the ratio of the BCC to FCC phases.[43] Because the energy of a magnetic particle in an external field is proportional to its volume (via the number of magnetic molecules), it decreases as the cube of the linear particle dimension. The large surface-to-volume ratio for small particles can also lead to decreased magnetization values. The magnetic molecules on the surface lack complete coordination. Finally, antiferromagnetic impurities like oxide and carbide can also decrease the total magnetization.[44]

Interestingly, from Slater-Paul curve, the M_s of bulk Fe-, Co-, Ni-based bulk alloys should locate between the two pure components.[45] On the contrary, our results show that the bimetallic nanoparticles obtain the lowest M_s, which may result from the amorphous structure and the interaction between the two component atoms.

3.3 Discussion of electromagnetic measurement

3.3.1 Electromagnetic properties

The values of electromagnetic complex permittivity and permeability were calculated from the scattering parameters, such as S_{11} and S_{21}, using the transmission line method with the Nicolson–Ross–Weir algorithm. Magnetic losses are more effective and sensitive than

dielectric losses for microwave absorption. A small difference in permeability can even affect the microwave absorption properties of the materials.[34] The real part of relative complex permittivity and permeability are associated with the storage capability of electric and magnetic energies. The ε'' and μ'' are associated with energy loss within materials, resulting from dielectric and magnetic mechanisms such as conduction, resonance, interfaces, relaxation and atomic, electronic and/or dominant polarization.

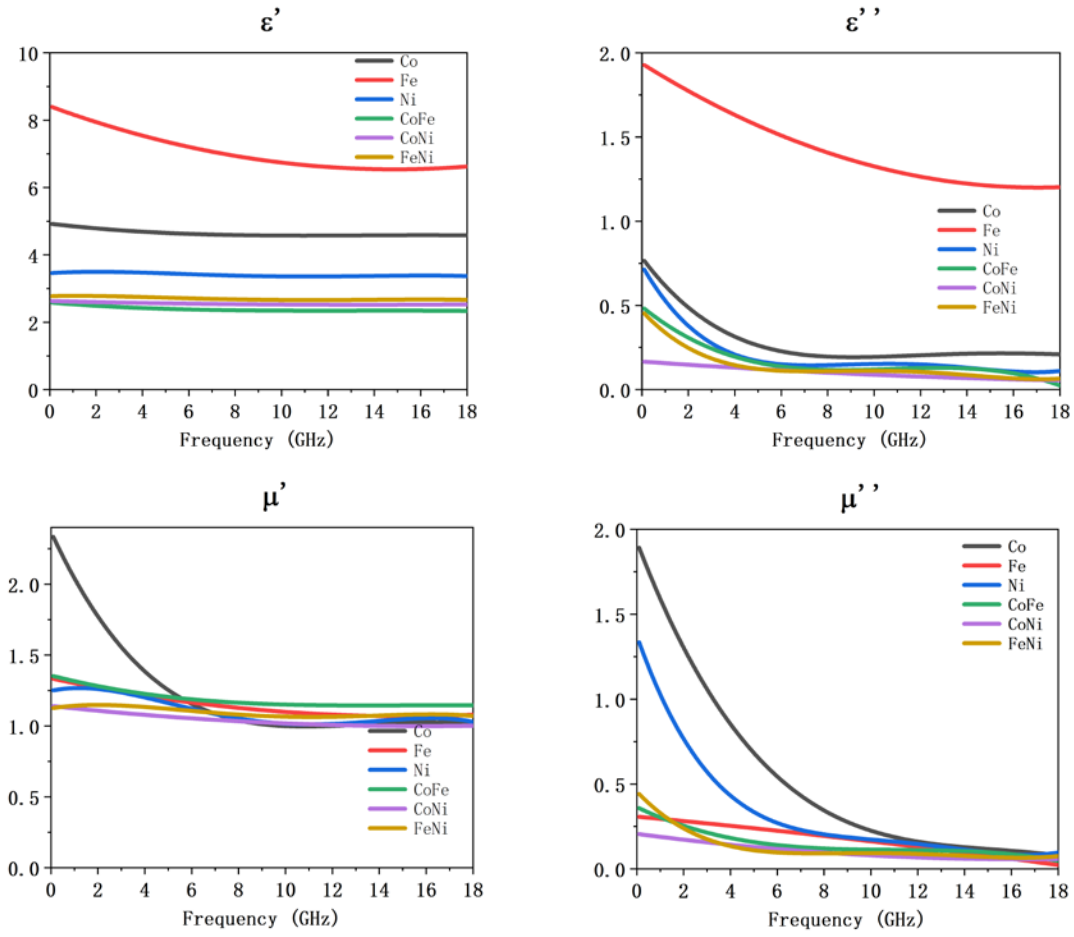

Figure 3.5 The real and imaginary part of permittivity and permeability for all nanoparticles at 30 vol% loading at 4 mm thickness.

In **Figure 3.5**, the real part of the permittivity (ε') of the specimens remained almost constant in the whole frequency range. The constancy means that there was a dominant polarization, in

which the oscillation of the electric dipole moments was in phase or somewhat out of phase with the microwave frequencies.[46] Moreover, the atomic and electronic polarizations may take place within a period shorter than the period of a microwave signal. Both the direct current conductivity and the alternating current conductivity may cause the dielectric loss of the materials. It can be seen clearly by the following equation:

$$\varepsilon'' = {}^{\sigma_{dc}}/_{(\omega\varepsilon_0)} + \varepsilon_{ac} \quad (3.1)$$

It appears that the direct current conduction loss is inversely proportional to the frequency; hence, the reason for the increase in ε'' for all samples with decreasing frequency at lower frequencies. The ε'' value exhibits a mild peak in the 10-14 GHz range, indicating a resonance behavior, which is expected when the sample is highly conductive. The nanoscale metal particles have a higher resistance which can contribute to lower polarization and dielectric loss.[47, 48] In this work, the low complex permittivity in the full frequency range also indicates that a high resistivity exists in the alloy nanoparticles, which may come from the thin shell of metal oxide on the nanoparticles.

Figure 3.5 also shows the frequency dependence of the relative complex permeability for the samples. It can be seen that from 2 – 18GHz, the real part and the imaginary part of permeability values (μ' and μ'') lie in the ranges 1.01-1.28 (except Fe) and 0.02-0.28 (except Fe and Ni), respectively. The small values of the latter suggest that the magnetic loss has a low contribution to electromagnetic wave attenuation. While for Fe nanoparticles, both μ' and μ'' have greater values than other samples.

As is well known, the relative permeability can be approximately expressed as[48]

$$\mu' = 1 + (M/H)\cos\sigma \quad (3.2)$$

$$\mu'' = 1 + (M/H)\sin\sigma \tag{3.3}$$

where M is the magnetization, H is the value of the external magnetic field, and σ is the phase lag angle of magnetization behind external magnetic field. According to the basic equations, it can be expected that the low permeability comes from the low magnetization. In the case of nanoparticles, the low magnetizations are attributed to the existence of nonmagnetic or weak magnetic oxide shells. It can also be proved that the magnetization of nanoparticles is saturated more slowly, owing to the superparamagnetism of the oxide shell. The μ_r'' of the CoFe and $FeNi_2$ exhibit resonance peaks in **Figure 3.5**, which are approximately located at 13.5, 11.0 GHz, respectively. The imaginary part of permeability reflects the magnetic loss which mainly comes from the magnetic hysteresis, domain-wall displacement, eddy current loss, and natural resonance. The hysteresis loss originating from the irreversible magnetization is negligible in a weak field.[49] The domain-wall resonance usually appears in the 1–100 MHz range in the multidomain materials and certainly is absent in the present single-domain nanoparticles. The eddy current loss is related to the electrical conductivity and the thickness of the samples. It can be expressed by X_{eddy}:[50]

$$X_{eddy} = 2\pi\mu_0\sigma d^2 \tag{3.4}$$

where μ_0 is the permeability value of a vacuum and σ is the electric conductivity of the material. For the nanosphere samples here, the high-frequency permeability of metallic magnetic materials may decrease due to losses from eddy current induced by the EM waves. Also, according to the theory of ferromagnetic resonance,[51] the natural resonance frequency is related to the anisotropy field that can be expressed by

$$f_r = \left(\frac{\gamma}{2\pi}\right) H_{eff} \tag{3.5}$$

where f_r is the resonance frequency, γ is the gyromagnetic ratio, and H_{eff} is the effective anisotropy field. The surface anisotropy in ferromagnetic nanoparticles originates from broken symmetry at the surface and becomes the main contributor to the effective anisotropy which enlarges the H_{eff}. Hence, the enhanced surface anisotropies in nanosized particles provide the essential contributions to the natural frequency.

It may be noted that the practical performance (RL value) of a RAM also requires good impedance matching properties between air and the material, which, in turn, are associated with the resultant complex permittivity and permeability. Small differences in permeability can even affect the microwave absorption properties of the materials.[52]

The dielectric (tan $\delta_\varepsilon = \varepsilon_r''/\varepsilon_r'$) and magnetic (tan $\delta_\mu = \mu_r''/\mu_r'$) loss tangent are represented in **Figure 3.6**. It is noted that the values of the magnetic loss tangent are generally larger than the dielectric loss tangent for all the nanoparticles samples, which means that the absorption originates mainly from the magnetic characteristics rather than the dielectric characteristics.

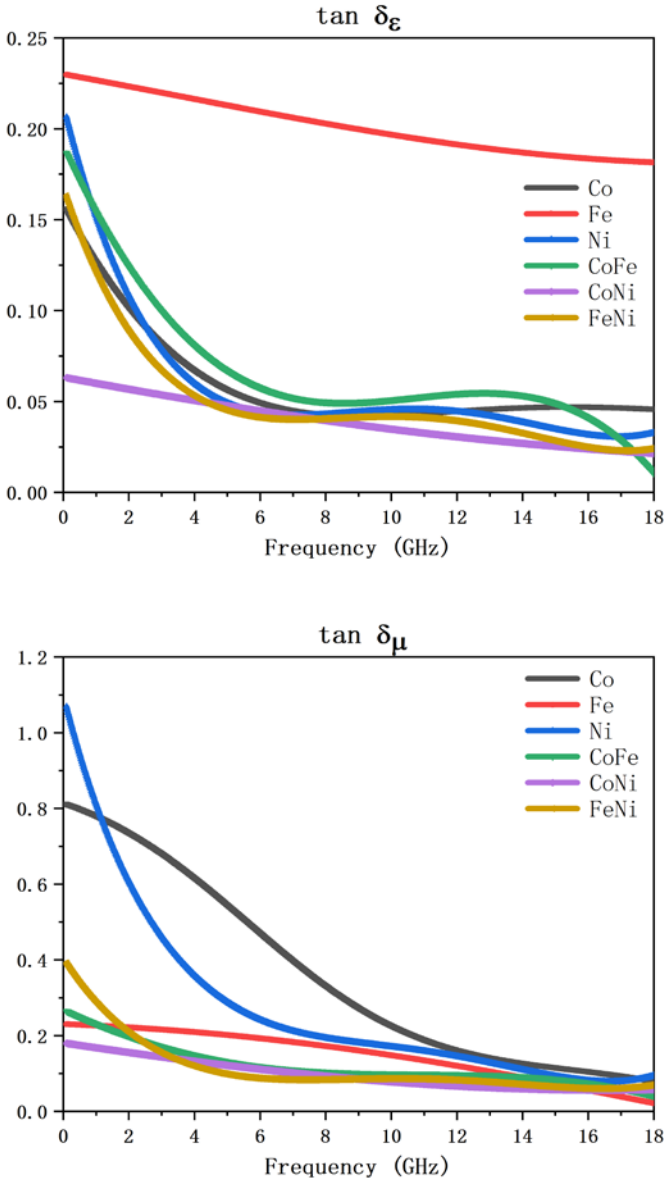

Figure 3.6 The dielectric (tan δ_ε) and magnetic (tan δ_μ) loss tangent of each sample.

3.3.2 Radar wave absorption properties

Figure 3.7 shows a typical data output using 10 nm Ni nanoparticles at a 30 vol% loading. **Figure 3.7(a)** shows the reflection loss (R_L) data for varying thicknesses (1 mm – 6 mm) of 10 nm Ni/paraffin wax composites at a 30 vol% nanoparticle loading. The relationship

between the reflection loss of the Ni/paraffin wax composite and frequency is calculated as follows:

$$Z_{in} = \sqrt{\mu_r/\varepsilon_r}\tanh(\mathrm{j}\frac{2\pi f d\sqrt{\mu_r\varepsilon_r}}{c}) \quad (3.6)$$

$$R_L = 20log\left|\frac{Z_{in}-1}{Z_{in}+1}\right| \quad (3.7)$$

where ε_r and μ_r are the relative complex permittivity and permeability of the wax composite, c is the speed of light, f is the frequency and d is the thickness of the absorbing material. As shown in **Figure 3.7(a)**, R_L absorption peaks for 10 nm Ni at a 30 vol% loading across all thickness on a 0.5 mm interval from 1 mm to 6 mm can be seen with a local maximum absorption of -6.59 dB at 5.98 GHz corresponding to the 6 mm thickness. It can be seen that when thickness decreases, the first absorption peak would shift to higher frequency (right shift) with a decreasing R_L. More intense electromagnetic wave absorption occurs at frequencies higher than our measurable range as the absorption reaches -5.13 dB at 18 GHz and keeps going down afterwards.

Figure 3.7(b) shows the real and imaginary portions of the complex permittivity and permeability across the frequency range from 2 GHz – 18 GHz for 10 nm Ni nanoparticles at a 30 vol% loading. In general, the values of both the real (ε', μ') and imaginary (ε'', μ'') portions of the complex permittivity and permeability gradually decrease with increasing frequency. For real portions, ε', a much sharper decrease can be seen early in the frequency range, from 2 GHz < f < 10 GHz.

Similarly, **Figure 3.8** shows a typical data output using 10 nm Co nanoparticles at a 30 vol% loading. As shown in **Figure 3.8(a)**, R_L absorption peaks for 10 nm Co at a 30 vol% loading can be seen with a local maximum absorption of -16.97 dB at 4.53 GHz corresponding to the

6 mm thickness. The values of ε', μ', ε'', μ'' for 10 nm Co nanoparticles at a 30 vol% loading gradually decrease with increasing frequency. For permeability, μ' and μ', a much sharper decrease can be seen early in the frequency range, from 2 GHz < f < 7 GHz.

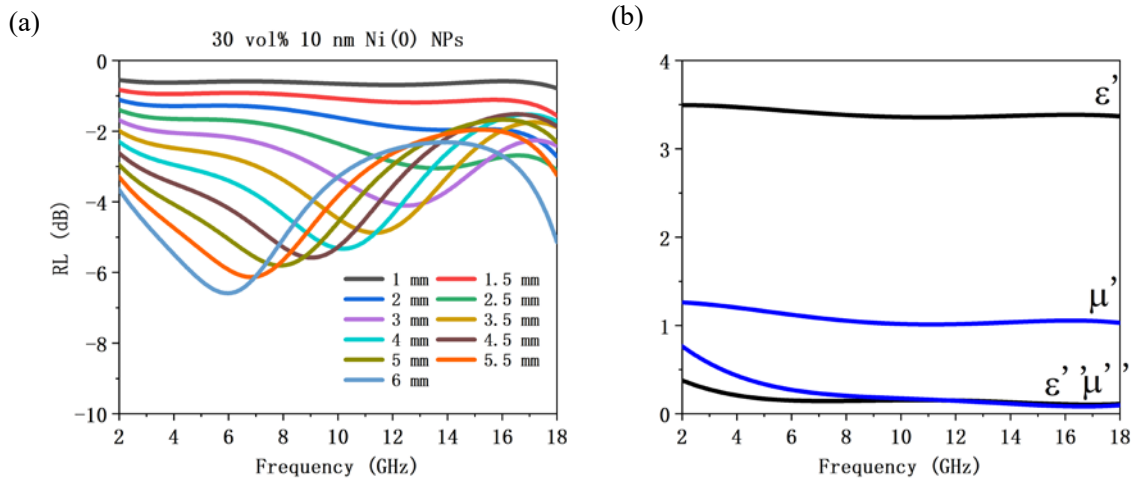

Figure 3.7 (a) Reflection loss for varying thicknesses (1 mm – 6 mm) of 10 nm Ni/paraffin wax composites at 30 vol% nanoparticle loading. (b) Permittivity and permeability values for 10 nm Ni/paraffin wax composites at a 1 mm thickness.

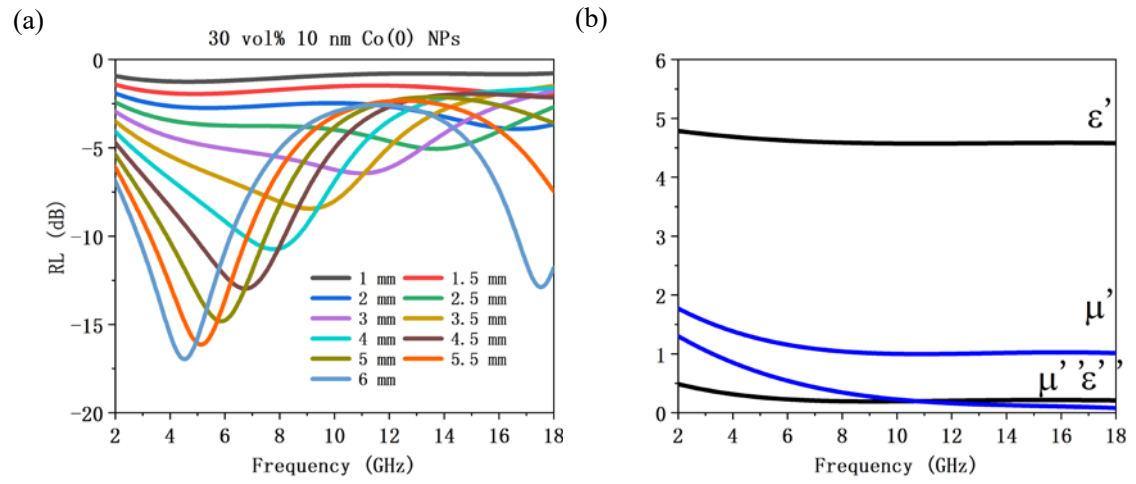

Figure 3.8 (a) Reflection loss for varying thicknesses (1 mm – 6 mm) of 10 nm Co/paraffin wax composites at 30 vol% nanoparticle loading. (b) Permittivity and permeability values for 10 nm Co/paraffin wax composites at a 1 mm thickness.

The effects of loading dependence on the materials properties and reflection loss data of the system were measured at varying loadings of 15, 30 and 40 vol% for all nanoparticle samples and the data analyzed for trends. **Figure 3.10** shows the effect of nanoparticle loading on the intensity of electromagnetic wave absorption (**Figure 3.10(a)**), the permittivity, and the permeability (**Figure 3.10(b)**) of 10 nm Ni nanoparticles in a toroid of 4 mm thickness. In agreement with previous studies of our own and others, it is shown that as nanoparticle loading increases, ε' and ε'' increase as well while μ' and μ'' only fluctuate a little. The reasoning behind this phenomenon is explained by the fact that as the loading of the sample increases, the overall volume of nanoparticles increases as well, thus increasing the effective permittivity of the material. The maximum absorption frequency decreases as the loading increases, while the intensity shows no clear trend. The discrepancy mainly comes from the μ'' and ε''. At frequency lower than 9 GHz, 30 vol% and 40 vol% have similar μ'' and ε'', thus the absorption intensity of two samples are close. After 9 GHz, because 30 vol% sample owns higher μ'' and ε'', both dielectric and magnetic loss increase. According to Bruggeman Effective Medium Theory as **Figure 3.9**, if we mix the inclusion with higher μ into the host matrix with low μ, the overall effective μ would locate in between each component.

$$v\frac{\mu_i - \mu_{eff}}{\mu_i + 2\mu_{eff}} + (1 - v)\frac{\mu_m - \mu_{eff}}{\mu_m + 2\mu_{eff}} = 0 \tag{3.8}$$

Where μ_i is intrinsic permeability of magnetic NPs, μ_m is permeability of the host matrix, v is the inclusion volume fraction in the matrix and μ_{eff} is effective permeability of the NPs/wax composite. The effective permeability is the permeability of the NPs/wax composite, in our case, it is the μ we measure. When the intrinsic permeability of the magnetic NPs remains constant, and the permeability of the wax is constant and lower than the NPs, the effective μ

is associated with the volume fraction of the inclusion NPs. We rearrange the EMT and have the Equation here. It's clear that as the *v* increases, the μ_{eff} increases.

$$v = \frac{2\mu_{eff}}{3(\mu_i - \mu_m)} - \frac{\mu_i \mu_m}{3(\mu_i - \mu_m)\mu_{eff}} + \frac{\mu_i - 2\mu_m}{3(\mu_i - \mu_m)} \tag{3.9}$$

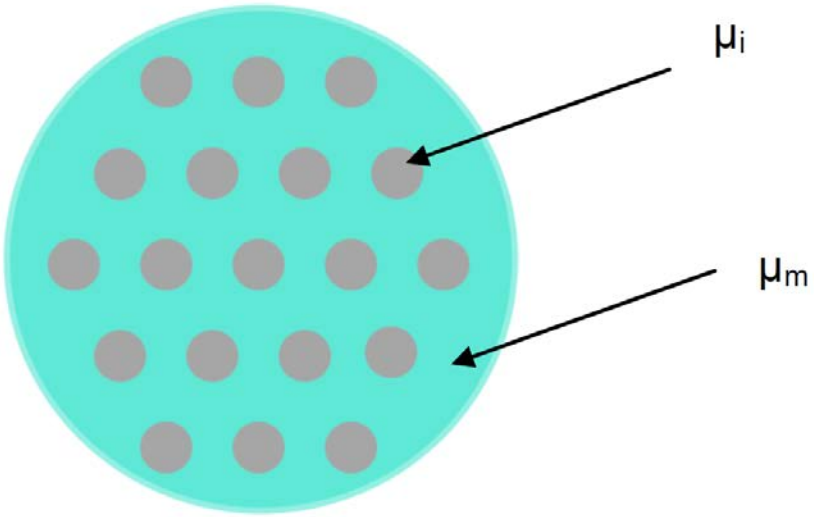

Figure 3.9 A schematic representation of particles embedded in matrix

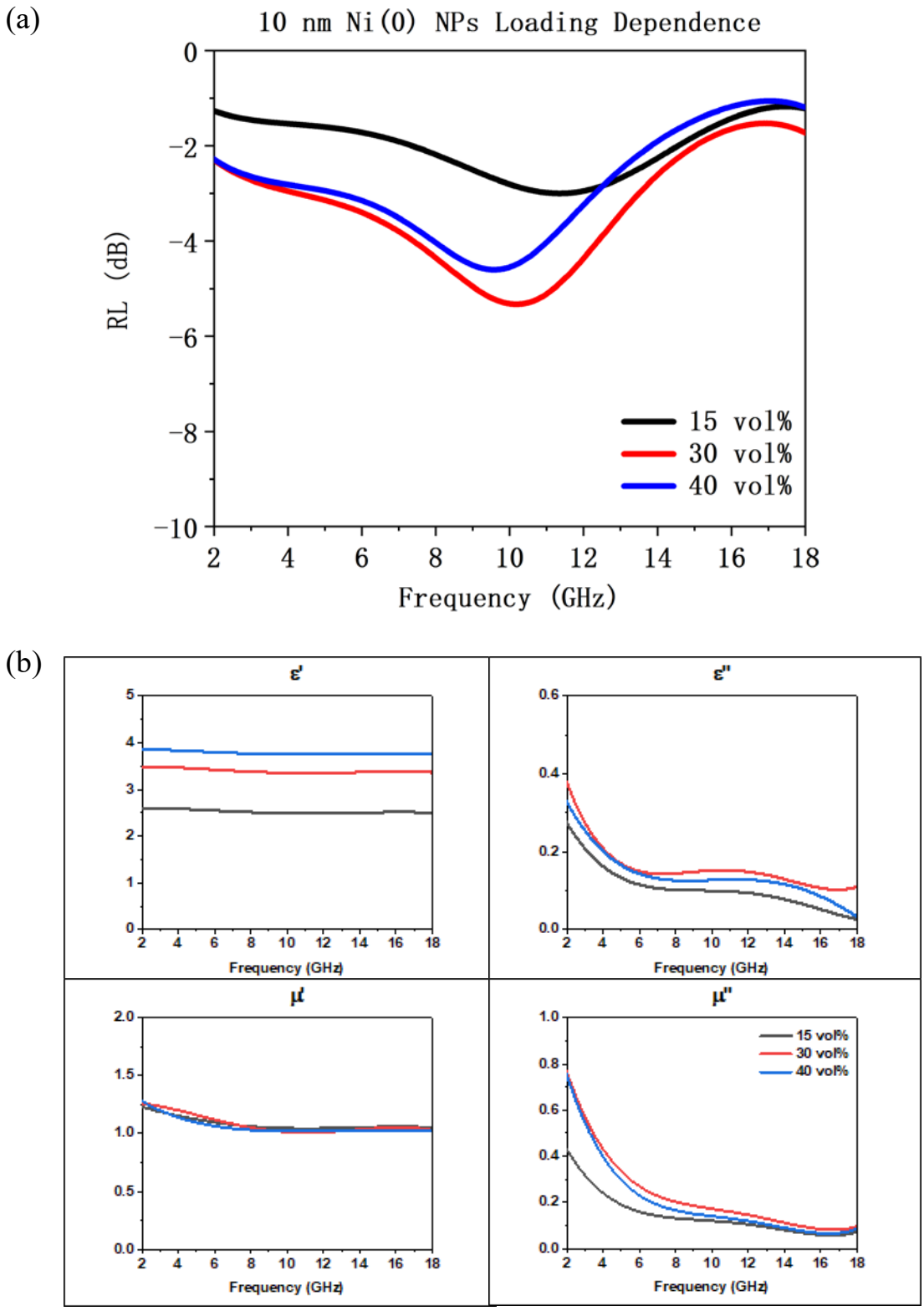

Figure 3.10 (a) Reflection loss for varying nanoparticle loadings (15, 30, and 40 vol%) of 10 nm Ni/paraffin wax composites at a 4 mm thickness. (b) Visualization of the effect of loading on the real and imaginary portions of the permittivity and permeability of 10 nm Ni nanoparticles.

Table 2 and **3** summarize the frequency and maximum absorption intensity for 4 mm thick wax/nanoparticle composite across all loadings. However, there is no clear trend for all samples in neither frequency nor intensity corresponding to loading. Electromagnetic properties highly depend on the particle size and interaction between particles, on which the samples preparation has great influence.

Table 2. Nanoparticles Loading Effects on Frequency of Electromagnetic Wave Absorption

Loading	**Fe**	**Co**	**Ni**	**CoFe**	**$FeNi_2$**	**CoNi**
15 vol%	8.51 GHz	7.44 GHz	11.33 GHz	10.82 GHz	12.05 GHz	11.60 GHz
30 vol%	6.77 GHz	7.80 GHz	10.21 GHz	12.79 GHz	11.60 GHz	11.65 GHz
40 vol%	6.92 GHz	7.95 GHz	9.63 GHz	12.25 GHz	11.02 GHz	11.53 GHz

Table 3. Nanoparticles Loading Effects on Absorption Intensity of Electromagnetic Wave Absorption

Loading	**Fe**	**Co**	**Ni**	**CoFe**	**$FeNi_2$**	**CoNi**
15 vol%	-9.26 dB	-6.54 dB	-3.00 dB	-1.68 dB	-3.06 dB	-3.12 dB
30 vol%	-16.94 dB	-10.74 dB	-5.33dB	-3.07 dB	-2.72 dB	-2.12 dB
40 vol%	-16.35 dB	-16.38 dB	-4.60 dB	-4.84 dB	-3.54 dB	-2.22 dB

3.3.3 Thickness dependence of R_L peak

Based on the transmission line theory, the reflection coefficient *r* of an EM wave entering from free space into a material with a flat surface can be written as Equation (1.13) and to achieve maximum reflection of the EM wave, the *r* should be equal to zero which is called impedance matching condition, therefore we got Equation (1.15). To further simplify this

equation, we assume the loss comes entirely from magnetic loss then we have the relationship between thickness *d* and R_L frequency. For **Figure 3.8(a)**, the data is listed int the **Table 4**, and it's clear that when μ'' of Co NPs holds constant, as *d* increases, frequency decreases.

Table 4. **Peak dependence on thickness of 30% Co NPs**

d (mm)	1	1.5	2	2.5	3	3.5	4	4.5	5	5.5	6
peak (GHz)	-	17.64	16.68	13.73	11.02	9.12	7.80	6.72	5.87	5.13	4.53

3.3.4 Alloying effect

Figure 3.11 shows all metallic samples have better EM wave absorbing ability than bimetallic alloys since the reflection loss are greater. Fe, Co, and Ni nanoparticles all obtain the loss peak below -5 dB while other samples hardly have any effect.

Take Co, Ni and CoNi nanoparticles as an example. They vary from each other in reflection loss and complex permittivity (**Figure 3.12**). The alloy's absorption intensity (-2.12 dB) is much weaker comparing with Co (-10.74 dB) and Ni (-5.33 dB). Furthermore, the peak frequency of CoNi (11.65 GHz) is greater than Co (7.80 GHz) and Ni (10.21 GHz).

The ε' of all samples are almost independent of frequency in the whole frequency range, indicating the coexistence of the multiple polarization mechanisms in the nanoparticles. The Co and Ni samples show a decreasing ε'' at frequency < 5 GHz, which agrees with Equation (3.1). However, CoNi alloy presents a much lower ε' indicating poor conductivity[53], probably due to heavier oxidation which blocks the formation of an electric conducting network. For complex permeability, both μ' and μ'' of Co decrease sharply from 2 GHz to

around 8 GHz. The μ' of all samples merge after 8 GHz. The μ'' of Co and Ni intersect at around 11 GHz, which agrees with the R_L curve (intersection of Co and Ni locates at 10.77 GHz). They are greater than CoNi through the whole frequency range. Although there is difference in complex permittivity, at high frequency (> 15.4 GHz) the absorption behavior of three samples converge as the complex permeability does. The dielectric ($\tan\delta_\varepsilon$) and magnetic ($\tan\delta_\mu$) loss tangents (**Figure 3.13**) of all samples also confirm that the magnetic loss is the main mechanism for the radar wave absorption.

It can be found that the values of μ'' and resonance peaks vary with the alloy components, which can be attributed to the variation in the magnetrocrystalline anisotropies according to the expression:

$$\mu'' \propto M_S^2/|K_1| \tag{3.10}$$

where K_1 is the first-order magnetrocrystalline anisotropy constant.[48] Considering CoNi has the lowest M_s, it is reasonable for CoNi to give a poorest absorption.

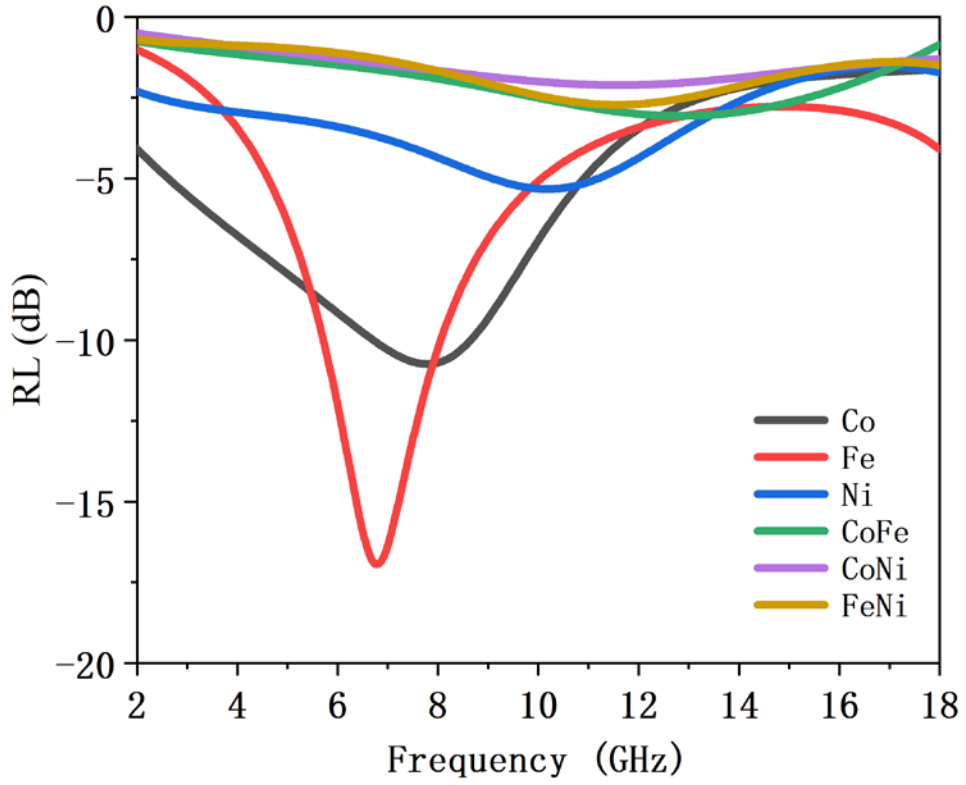

Figure 3.11 Illustration of the effect of alloying on the reflection loss resonant frequency for samples of 4 mm thickness and 30 vol% loading.

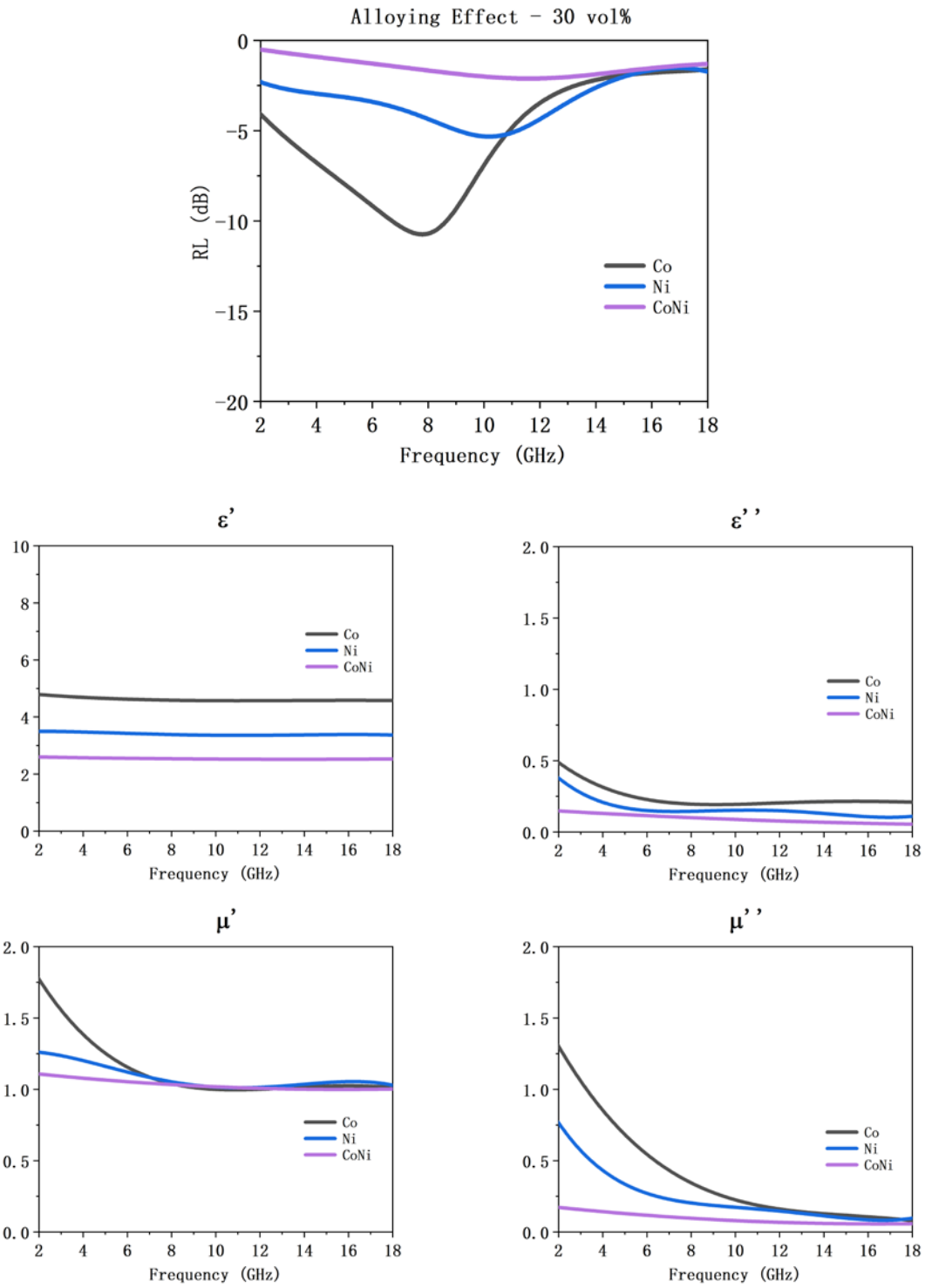

Figure 3.12 Illustration of the effect of alloying on the reflection loss resonant frequency for Co, Ni and CoNi of 30 vol% loading.

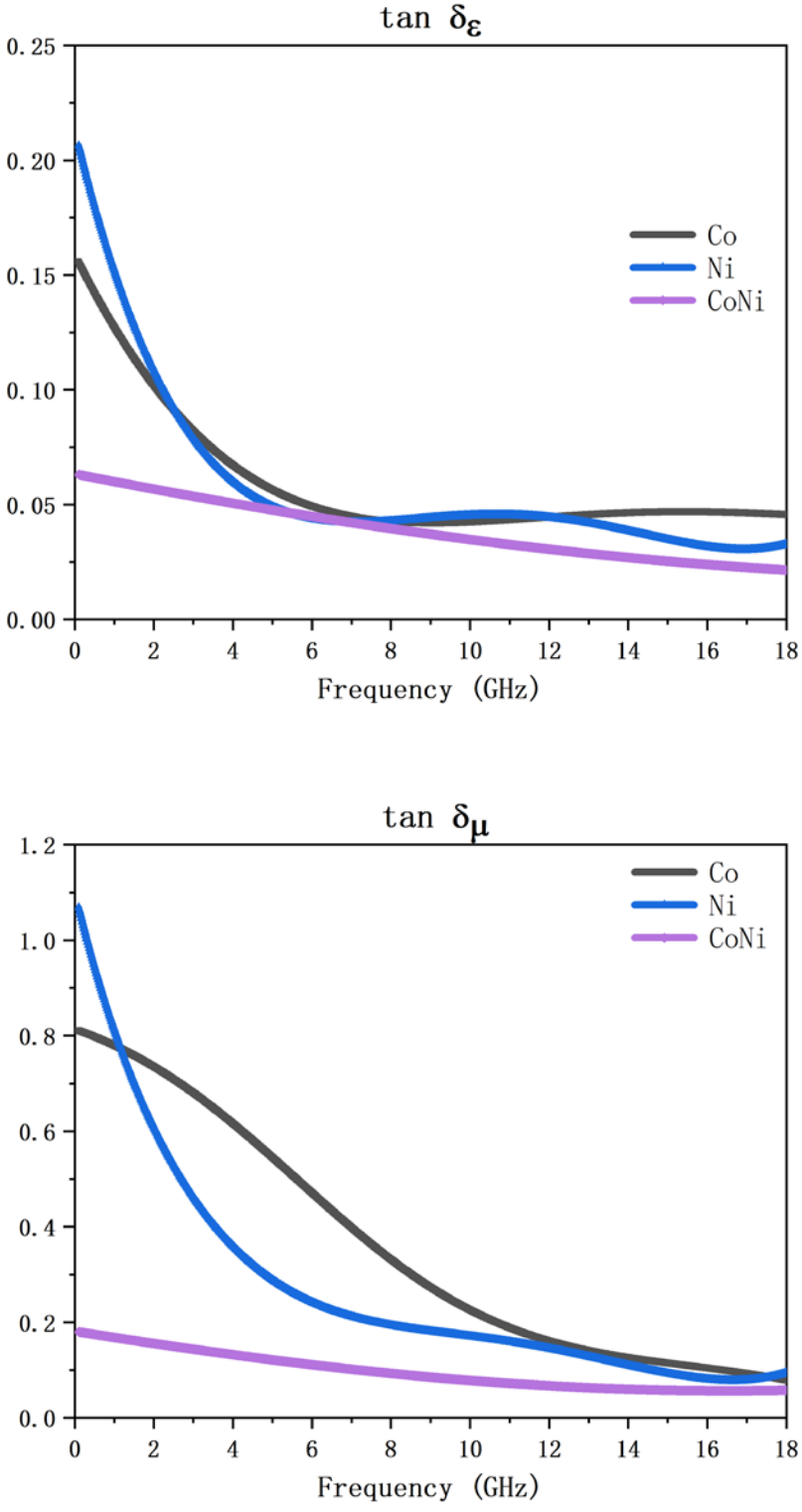

Figure 3.13 The dielectric (tan δ_{ε}) and magnetic (tan δ_{μ}) loss tangent of each sample.

4. Conclusion and future steps

Our study presents some fundamental principles of EM wave absorption. Based on particle structures and their magnetic properties, the complex permeability and the EM wave absorption properties can be analyzed and predicted. We have synthesized uniform M(0) magnetic NPs and magnetic loss is the main mechanism by which these NPs absorb the EM wave, where complex permeability has dominant influence. Electromagnetic properties were studied to understand the RL dependence on loading and thickness and our results fit the theory.

To take a step further, we study the alloying effect on NPs while these alloy NPs do not follow the trend we derived from M(0) NPs. In the future, more work needs to be completed on characterizing the magnetic properties of M (0) and alloyed NPs including M_S and H_C and compare with their bulk counterparts and characterizing the structure of the alloyed NPs and understand the correlation between their structures and magnetic properties. Finally, we can develop novel EM wave absorbers by tailoring the structure and electromagnetic properties.

5. References

1. Edwards, M., *Land-based military applications.* 2000.
2. Teber, A., *Development of Radar Absorbing Materials (RAMs) based on Nano-Structured Magnetic Materials and Applications.* 2017.
3. Petrescu, R.V., et al., *Lockheed martin-a short review.* Journal of Aircraft and Spacecraft Technology, 2017. **1**(1).
4. Council, N.R., *Identification of research needs relating to potential biological or adverse health effects of wireless communication devices*. 2008: National Academies Press.
5. Seidenberg, E. and H. Schimpf. *Aspects of automatic target recognition with a two-frequency millimeter-wave SAR*. in *Radar Sensor Technology V*. 2000. International Society for Optics and Photonics.
6. Ahlbom, A., et al., *Possible effects of electromagnetic fields (EMF) on human health--opinion of the scientific committee on emerging and newly identified health risks (SCENIHR).* Toxicology, 2008. **246**(2-3): p. 248-250.
7. Ghosh Chaudhuri, R. and S. Paria, *Core/shell nanoparticles: classes, properties, synthesis mechanisms, characterization, and applications.* Chemical reviews, 2011. **112**(4): p. 2373-2433.
8. Peng, Y.-h., et al., *Study on synthesis of ultrafine Cu–Ag core–shell powders with high electrical conductivity.* Applied Surface Science, 2012. **263**: p. 38-44.
9. Aktsipetrov, O., *Nonlinear magneto-optics in magnetic nanoparticles.* Colloids and Surfaces A: Physicochemical and Engineering Aspects, 2002. **202**(2-3): p. 165-173.
10. Lin, X.-M. and A.C. Samia, *Synthesis, assembly and physical properties of magnetic*

nanoparticles. Journal of Magnetism and Magnetic Materials, 2006. **305**(1): p. 100-109.

11. Dai, Q. and A. Nelson, *Magnetically-responsive self assembled composites.* Chemical Society Reviews, 2010. **39**(11): p. 4057-4066.

12. Krishnan, K.M., et al., *Nanomagnetism and spin electronics: materials, microstructure and novel properties.* Journal of materials science, 2006. **41**(3): p. 793-815.

13. Ganguly, R. and I.K. Puri, *Field-assisted self-assembly of superparamagnetic nanoparticles for biomedical, MEMS and BioMEMS applications.* Advances in applied mechanics, 2007. **41**: p. 293-335.

14. Wang, J.-P., *FePt magnetic nanoparticles and their assembly for future magnetic media.* Proceedings of the IEEE, 2008. **96**(11): p. 1847-1863.

15. Singamaneni, S., et al., *Magnetic nanoparticles: recent advances in synthesis, self-assembly and applications.* Journal of Materials Chemistry, 2011. **21**(42): p. 16819-16845.

16. Lu, A.H., E.e.L. Salabas, and F. Schüth, *Magnetic nanoparticles: synthesis, protection, functionalization, and application.* Angewandte Chemie International Edition, 2007. **46**(8): p. 1222-1244.

17. Park, J., et al., *Ultra-large-scale syntheses of monodisperse nanocrystals.* Nature materials, 2004. **3**(12): p. 891.

18. Sun, S., et al., *Monodisperse mfe2o4 (m= fe, co, mn) nanoparticles.* Journal of the American Chemical Society, 2004. **126**(1): p. 273-279.

19. Redl, F.X., et al., *Magnetic, electronic, and structural characterization of nonstoichiometric iron oxides at the nanoscale.* Journal of the American Chemical Society, 2004. **126**(44): p. 14583-14599.

20. Byun, M., J. Wang, and Z. Lin, *Massively ordered microstructures composed of magnetic nanoparticles.* Journal of Physics: Condensed Matter, 2009. **21**(26): p. 264014.

21. Jana, N.R., Y. Chen, and X. Peng, *Size-and shape-controlled magnetic (Cr, Mn, Fe, Co, Ni) oxide nanocrystals via a simple and general approach.* Chemistry of materials, 2004. **16**(20): p. 3931-3935.

22. Puntes, V.F., K.M. Krishnan, and A.P. Alivisatos, *Colloidal nanocrystal shape and size control: the case of cobalt.* Science, 2001. **291**(5511): p. 2115-2117.

23. Murray, C., C. Kagan, and M. Bawendi, *Self-organization of CdSe nanocrystallites into three-dimensional quantum dot superlattices.* Science, 1995. **270**(5240): p. 1335-1338.

24. Murray, C., et al., *Monodisperse 3d transition-metal (Co, Ni, Fe) nanoparticles and their assembly intonanoparticle superlattices.* Mrs Bulletin, 2001. **26**(12): p. 985-991.

25. Dumestre, F., et al., *Shape control of thermodynamically stable cobalt nanorods through organometallic chemistry.* Angewandte Chemie International Edition, 2002. **41**(22): p. 4286-4289.

26. Dumestre, F., et al., *Unprecedented crystalline super-lattices of monodisperse cobalt nanorods.* Angewandte Chemie International Edition, 2003. **42**(42): p. 5213-5216.

27. Cordente, N., et al., *Synthesis and magnetic properties of nickel nanorods.* Nano letters, 2001. **1**(10): p. 565-568.

28. Peng, Z. and H. Yang, *Designer platinum nanoparticles: Control of shape, composition in alloy, nanostructure and electrocatalytic property.* Nano Today, 2009. **4**(2): p. 143-164.

29. Saville, P., *Review of radar absorbing materials*. 2005, Defence Research and Development Atlantic Dartmouth (Canada).

30. Barbosa, U.F., J.P.M.C. Costa, and R. Chaitanya. *Analysis of Radar Cross Section and Wave Drag Reduction of Fighter Aircraft*. in *procedings of the AEROSPACE TECHNOLOGY CONGRESS*. 2016.

31. Knott, E.F., J.F. Schaeffer, and M.T. Tulley, *Radar cross section*. 2004: SciTech Publishing.

32. Chen, L.-F., et al., *Microwave electronics: measurement and materials characterization*. 2004: John Wiley & Sons.

33. Liu, P., et al., *Construction of CuS nanoflakes vertically aligned on magnetically decorated graphene and their enhanced microwave absorption properties.* ACS applied materials & interfaces, 2016. **8**(8): p. 5536-5546.

34. Jänis, A., et al. *Microwave absorbing properties of ferrite-based nanocomposites*. in *Behavior and Mechanics of Multifunctional and Composite Materials 2007*. 2007. International Society for Optics and Photonics.

35. Teber, A., et al., *Manganese and zinc spinel ferrites blended with multi-walled carbon nanotubes as microwave absorbing materials.* Aerospace, 2017. **4**(1): p. 2.

36. Takashima, T., T. Suzuki, and H. Irie, *Electrochemical carbon dioxide reduction on copper-modified palladium nanoparticles synthesized by underpotential deposition.* Electrochimica Acta, 2017. **229**: p. 415-421.

37. Liao, Q., R. Tannenbaum, and Z.L. Wang, *Synthesis of FeNi3 alloyed nanoparticles by hydrothermal reduction.* The Journal of Physical Chemistry B, 2006. **110**(29): p. 14262-14265.

38. Chen, Q. and Z.J. Zhang, *Size-dependent superparamagnetic properties of MgFe 2 O 4 spinel ferrite nanocrystallites.* Applied physics letters, 1998. **73**(21): p. 3156-3158.

39. Batlle, X., et al., *Magnetic study of M-type doped barium ferrite nanocrystalline powders.* Journal of applied physics, 1993. **74**(5): p. 3333-3340.

40. Goya, G.F., et al., *Static and dynamic magnetic properties of spherical magnetite nanoparticles.* Journal of applied physics, 2003. **94**(5): p. 3520-3528.

41. Matsuura, H., et al., *Influence of oxidation and size of iron nanoparticles on the saturation magnetization.* IEEE Transactions on Magnetics, 2008. **44**(11): p. 2804-2807.

42. Kura, H., M. Takahashi, and T. Ogawa, *Synthesis of monodisperse iron nanoparticles with a high saturation magnetization using an Fe (CO) x− oleylamine reacted precursor.* The Journal of Physical Chemistry C, 2010. **114**(13): p. 5835-5838.

43. Moghimi, N., et al., *Shape-dependent magnetism of bimetallic FeNi nanosystems.* Journal of Materials Chemistry C, 2014. **2**(31): p. 6370-6375.

44. Shafi, K.V., et al., *Preparation and magnetic properties of nanosized amorphous ternary Fe–Ni–Co alloy powders.* Journal of Materials Research, 2000. **15**(2): p. 332-337.

45. Schoen, M.A., et al., *Magnetic properties of ultrathin 3 d transition-metal binary alloys. I. Spin and orbital moments, anisotropy, and confirmation of Slater-Pauling behavior.* Physical Review B, 2017. **95**(13): p. 134410.

46. Ahmad, S.H., et al., *Magnetic and microwave absorbing properties of magnetite–thermoplastic natural rubber nanocomposites.* Journal of Magnetism and Magnetic Materials, 2010. **322**(21): p. 3401-3409.

47. Deng, Y., et al., *Preparation and microwave characterization of submicrometer-sized hollow nickel spheres.* Journal of magnetism and magnetic materials, 2006. **303**(1): p. 181-184.

48. Lu, B., et al., *Influence of alloy components on electromagnetic characteristics of core/shell-*

type Fe–Ni nanoparticles. Journal of Applied Physics, 2008. **104**(11): p. 114313.

49. Wu, M., et al., *Microwave magnetic properties of Co 50/(SiO 2) 50 nanoparticles.* Applied Physics Letters, 2002. **80**(23): p. 4404-4406.

50. Yin, Y., et al., *Enhanced high-frequency absorption of anisotropic Fe 3 O 4/graphene nanocomposites.* Scientific reports, 2016. **6**: p. 25075.

51. Kittel, C., *On the theory of ferromagnetic resonance absorption.* Physical Review, 1948. **73**(2): p. 155.

52. Zhao, H.-B., et al., *Excellent electromagnetic absorption capability of Ni/carbon based conductive and magnetic foams synthesized via a green one pot route.* ACS applied materials & interfaces, 2016. **8**(2): p. 1468-1477.

53. Li, N., C. Hu, and M. Cao, *Enhanced microwave absorbing performance of CoNi alloy nanoparticles anchored on a spherical carbon monolith.* Physical Chemistry Chemical Physics, 2013. **15**(20): p. 7685-7689.

Shi Zhang

3900 N Charles St. Apt 603 | szhang91@jhu.edu | (443)716-8073

EDUCATION

Johns Hopkins University **08/2017-05/2019**
Master of Science in Chemical and Biomolecular Engineering

Nanjing University **09/2013-05/2017**
Bachelor of Science in Chemistry

RESEARCH EXPERIENCE

Johns Hopkins University

Tailoring of Magnetic Nanomaterials for Electromagnetic Wave Absorption
Advisor: Dr. Chao Wang 10/2017-Present

Aims: Develop and explore a fundamental understanding of the application of magnetic nanomaterials for electromagnetic wave absorption. We have been able to synthesize different nanoparticles to tailor the magnetic properties in terms of coercivity (H_c) and magnetization (M_0) and evaluate the dependence of the permittivity (ε) and permeability (μ) of the nanoparticle.

- Tailor nanoparticle morphologies in order to elucidate the underlying mechanisms behind EM wave absorption phenomenon.
- Synthesize different metal/alloy nanoparticles through organic solution thermal decomposition.
- Characterize the nanoparticles with TEM, XRD, EDS, VNA

Nanjing University

Research on the magnetism of Lanthanide-crown ether complexes
Advisor: Dr. You Song 10/2016-05/2017

- Prepared single lanthanide ion magnets, most of which show slow magnetic relaxation processes associated with SMM behavior.
- Studied lanthanide ions' slow magnetic relaxation process and photomagnetism, along with the development of photomagnetic switch.
- Investigated the effects of different lanthanide ions on SMM performance by SC-XRD and VSM.

Highly Sensitive Photoelectrochemical Biosensing Based on Functional Semiconductor Nanomaterials
Advisor: Dr. Junjie Zhu 09/2014-06/2015

- Took charge of the synthesis and characterization of precursor materials like Ag nanocubes and Au nanocages;
- Involved in the characterization and testing of in-process product
- Acquired the breadth of knowledge in nanomaterials especially quantum dots, quantitative ideas and experimental techniques of analytical chemistry, theory and techniques of biosensing and electrochemistry.

Design and Synthesis of Molecule-Based Magnets by Spin Frustration
Advisor: Dr. You Song 09/2015-09/2016

- Mainly constructed the Cu-W crystal clusters by using $W(CN)_8$ ion to create new single molecular magnets.
- Tested its magnetic properties to get a deeper understand of spin frustration and explored its functions in the practical application.

TECHNICAL SKILLS AND LANGUAGES

Languages: English (proficient), Chinese (native)
Experimental Skills: proficient in a variety of chemical experimental instruments and measuring methods such as glovebox, IR, UV, HPLC, NMR, TEM, XRD, EDS and VNA
Proficient in Origin, ImageJ, ChemOffice, Endnote, C Language, Python, Fortran, MC Office